Master Thesis in Geographical Information Science nr 177

Temporal RX-algorithm performance on Sentinel-2 images.

Martin Storsnes

2024
Department of
Physical Geography and Ecosystem Science
Centre for Geographical Information Systems
Lund University
Sölvegatan 12
S-223 62 Lund
Sweden

Martin Storsnes (2024) Temporal RX-algorithm performance on Sentinel-2 images.

Master's degree thesis, 30 credits in Master in Geographical Information Science
Department of Physical Geography and Ecosystem Science, Lund University

Temporal RX-algorithm performance on Sentinel-2 images.

Martin Storsnes
Master thesis, 30 credits, in Geographical Information Sciences

Supervisor: Anders Ahlström PhD
GIS Centre
Dept of Physical Geography and Ecosystem Science Lund University

Supervisor: Thomas Olsvik Opsahl
Norwegian Defence Research Establishment

Acknowledgements

I would like to thank my supervisors Anders and Thomas for their help and support. This assignment would not have been possible without. The possibility to be co-located with you and your colleagues, Thomas, has been a privilege, and I would like to thank everyone who has been involved in the process to make this happen.

I am also very pleased to have an employer that has given me a short leave to write this thesis. Dyre and Per Aslak, thank you. I would also like to thank Thomas G. and Bjørn who helped me with the application for this programme.

To my family, thank you for all your support during this process. Thinking straight is so much easier when surrounded by extraordinarily nice people.

Abstract

The increasing availability of satellite images with seemingly ever increasing spatial, spectral, and temporal resolution is a treasure when searching for information about activity on the surface of the earth. However, the large amount of data is challenging for humans to search through. Anomaly detection in time series of satellite images could potentially help humans to search specific areas for interesting changes reduce the workload on humans.

The RX-algorithm is commonly used for spatial anomaly detection, but there are not that many publications concerning the RX-algorithm applied on temporal data. The studies which have been done are on desert areas, which is assumed to be less challenging than the area in this thesis.

By changing the direction of the data sampling from spatial, meaning sampling of several pixels in the *x, y* direction of one satellite image, to the temporal direction meaning pixels with the same *x, y* location from several images taken at different times, the algorithm can be used for temporal anomaly detection.

In this thesis the performance of the temporal RX-algorithm is assessed by applying it on a time series of Sentinel-2 images and comparing the algorithms classification against the classification made by a human. All the classifications are binary, in this assignment meaning that it is either no change detected or change detected.

Spectral analysis of pixels with 10x10 meter resolution is challenging, and the quality of the data is crucial for the results. Mixed pixels, co-registration errors and scattered irradiance are present to some extent in all satellite images. The areas selected for this study are chosen to test the performance in areas where these errors are likely to be present.

Confusion matrixes are used to interpret the performance by analyzing the number of true positives and negatives, and false positives and negatives. It does also keep the spatial location of the performance metrics, so that the position of the errors could be analyzed. This indicates which type of errors that the misclassification could be caused by. The temporal dimension is tracked, and when in time the anomalies are introduced is visible in figures which can be compared to the corresponding image.

This project aims to broaden the understanding of the temporal RX-algorithm´s performance on time series of satellite images where the environment is more complex than a desert. It will hopefully shed light on the limitations and possibilities for such automated approaches to anomaly detection that could possibly aid humans when interpreting images in the search of anomalies with unknown spectral signatures.

Page intentionally left blank

Table of contents

List of figures

List of tables

List of equations

List of abbreviations

ACD	Anomaly Change Detection
AVOCADO	The Anomaly Vegetation Change Detection algorithm
CFAR	Constant False Alarm Rate
EO	Electro-Optical
IR	Infrared
MSI	Multi-Spectral-Instrument
NDVI	Normalized Difference Vegetation Index

PUT	Pixel Under Test
RGB	Red, Green, Blue.
RX	Reed-Xiaoli (algorithm)
TOA	Top of Atmosphere

1. Introduction

The use of remote sensing for monitoring large areas is not new, and 50 years of satellite imagery is available for this purpose (Decuyper, et al., 2022). The technological advances since the 1990s have made multi- and hyperspectral images from air- and spaceborne sensors increasingly valuable due to the high level of information they contain. Among the applications of this data, the monitoring of changes is useful and common (Wu, Zhang, & Du, 2015).

Change detection is to compare an image with multispectral measurements from a specific location with another and determine if the measurements have changed significantly. A significant change in the measurements implies that the observed location contains a change, while smaller changes could be due to differences in recording conditions (Singh, 1989). Change detection have a range of applications within planning, monitoring and surveillance of larger geographical areas (İlsever, 2012).

First, landcover changes were identified by using bi-temporal images, and later on with longer time series. When imagery is applied to monitoring of vegetation, it is common to use vegetation indices, such as the Normalized Difference Vegetation Index (NDVI), to detect and classify vegetation.

The Anomaly Vegetation Change Detection (AVOCADO) algorithm (Decuyper, et al., 2022) is recently developed to monitor deforestation and regrowth over time. The algorithm uses measurements of known undisturbed vegetation from nearby areas as reference vegetation. The measured values from these areas are used as input, and the algorithm accounts for seasonal changes to detect transitions in forest. The relevance of detection algorithms used on time series of data is shown with the AVOCADO algorithm, but the AVOCADO algorithm is specialized on vegetation and is probably too specific when you are searching for changes across different types of landcover containing different types of changes.

For surveillance purposes interesting landcover changes could be either temporary, here meaning appearing and disappearing, or permanent, here meaning changed from the original state to another permanent state. It is also important to discard changes assigned to normal variations and highlight actual changes in landcover. A change from one type of landcover to another, should be considered anomalous, while smaller changes between recordings of the same landcover at the same place should not be considered anomalous.

With the increasing availability of satellite imagery with high temporal, spatial and spectral resolution, the possibility to detect changes within the same pixel over time becomes increasing interesting for several types of automated surveillance systems.

In 1990 Irving Reed and Xiaoli Yu (Reed & Yu, 1990) introduced the Reed-Xiaoli (RX) algorithm for anomaly detection. This has since become one of the most common algorithms for spatial anomaly detection (Manolakis, 2002). In 2020 a slightly modified RX-algorithm was applied for temporal anomaly detection in a time series of co-registered multispectral images, proving that it can be used both spatially and temporally (Ziemann, Simonoko, & Flynn, 2020), (Simonoko, Ziemann, & Flynn, 2020).

It is possible to argue that temporal anomaly detection is both anomaly detection and anomaly change detection since it detects anomalies rather than anomalous changes, but since the time of a change can be identified, the change can be identified.

In their research on Temporal RX, Ziemann et al. (Ziemann, Simonoko, & Flynn, 2020), (Simonoko, Ziemann, & Flynn, 2020) use images of a desert area taken between June and October 2018.

This study aims to investigate if the temporal RX-algorithm can be used to detect anomalous changes in a time series of co-registered multispectral images in a more challenging environment than desert. This study uses a collection of Sentinel-2 1C images from July 2015 to November 2022 of the 32VKP grid tile.

Sentinel-2 multi spectral images are used due to the assumed high quality of the post-processing of the images that should reduce errors and reduce the need of further processing steps. 1C products are used because the data was downloaded before the systematic provision of 2A products was made available (Esa, 2024). The focus is primarily on classification precision compared to a human made ground truth, focusing on false positives and negatives at 10x10 meter resolution.

The analysis is done on five patches containing nine pixels each. Performance is evaluated by comparing the classification of pixels done by visual interpretation and by the temporal RX-algorithm. The assignment aims to investigate if temporal anomaly detection on Sentinel-2 images with a resolution up to 10x10 meters is suitable for automatic detection of objects such as boats and windmills. If an automated process could replace, or aid, human visual interpretation of satellite images, the growing amount of data could still be analysed within a reasonable timeframe.

The thesis uses temporal samples of the same pixel location for a given span of time to create a statistical background model that later pixels in the time series are compared against. The statistical model for each pixel location is assumed to capture natural variations for that location over time. When a test pixel is compared to the model, it should fit fairly with the model if the content of the pixel is the same. If the pixel does not fit reasonably with the statistical model, an anomaly is detected. The detection of an anomaly gives us a reason to assume that the content within the pixel has changed.

Since the statistical model is drawn from a specified timeframe, it is possible to find the timestamp of the detected anomalies, and thru that detecting the change related to the initial model. If the pixel contains vegetation when the statistical model is created, but later is converted to a road, the anomalous change is when the pixel transitions from vegetation to road. However, the road will not be anomalous since the road is a new normal but the pixels containing road will be anomalous compared to the, now outdated, statistical model.

The thesis focuses on pixel level detection of anomalies over time to find changes and compares the automated classification against classification done by a human. The types of errors that occurs sheds light on which problems such types of systems must handle to deliver consistently good results.

1.1. Disposition

The thesis consists of this introduction with research objectives and questions, before the background is presented. The background presents the literature review and introduces the most important theory and facts about the subject and data this thesis draws upon. Then the methodology of the experiment is described in detail. Then the results are presented for each of the five patches individually, before a short overall performance is presented. This is followed by a discussion part where the results are debated, shortfalls within the research design are discussed and suggestions for

further research is presented. Finally, a conclusion is presented that states the answers to the research questions.

1.2. Research objectives and questions

This thesis aims to evaluate if the temporal RX algorithm is suitable for detecting anomalous changes in time series of Sentinel-2 images with a spatial resolution of 10x10 meters.

Assumptions:

1) If the data quality is consistent, significant changes in spectral measurements for pixels outside the timeframe of the statistical model should be detected.
2) The performance is dependent on the spatial size of the change. Ground changes not covering a full 10x10 meters pixel will likely give a higher false rate, than those bigger than 10x10 meters.

Objective 1: Investigate if the temporal RX-algorithm can detect different types of anomalous changes in a less homogenous environment than a desert with Sentinel-2 data.

Q1.1: Is the temporal RX-algorithm able to detect changes in Sentinel-2 data with other types of landcover than desert?

Q1.2: Are the timestamp of the anomalies that the temporal RX-algorithm detects consistent with the visually detectable changes in the Sentinel-2 images?

Objective 2: Assess the precision of detection at 10x10 meter spatial resolution on 3x3 pixel patches with different landcover and temporal anomalies.

Q2.1: How many false positives and negatives will the temporal RX-algorithm produce in each 3x3 pixel patch?

Q2.2: How is the spatial distribution of the false positives and negatives in each patch, and how do they relate to the shape of the change?

Page intentionally left blank

2. Background

2.1. Change detection

Change detection is used to identify physical changes on the surface of the earth by comparing satellite images of the same area taken at different times (Zhao, Shan, & Wang, 2023). Such changes could occur because of "[…] deforestation, disasters, urbanization, change in coarse of river, etc." (Elkholy, Mostafa, ElSayad, Ebeid, & Tolba, 2023), but the application of change detection is not restricted to landcover changes (Geethika, Sreeja, Tharuni, & Radhesyam, 2024). The movement of objects on the earth's surface, such as boats and cars, should also be possible to detect with change detection if the objects are larger than the image resolution.

The information change detection can provide is useful for decision making and could inform decisionmakers about urban expansion and changes in water bodies (Elkholy, Mostafa, ElSayad, Ebeid, & Tolba, 2023). It is also useful for mapping the extent of natural disasters (Zhao, Shan, & Wang, 2023), and how deforestation or other changes in vegetation are developing (Geethika, Sreeja, Tharuni, & Radhesyam, 2024).

The premise of change detection is that a change in landcover must result in a larger change in spectral signature captured by remote sensing than changes caused by other factors such as differences in atmospheric conditions, sun angle, soil moisture etc. (Singh, 1989). When comparing the spectral signatures measured at the same location recorded at different times, identification of changes significantly larger than background noise can be used to detect landcover change.

Change detection is a difficult task (Acito, Diani , Corsini, & Resta, 2017), and many different methods have been developed. Some methods are better suited for some applications, while others are better suited for other applications. The methods here are not comprehensive but gives an overview of some of the most common methods. Lu et al. (Lu, Moran, Mausel, & Brondízio, 2004) published an article with a review of different change detection methods and divided them into seven main categories: algebra, transformation, classification, advanced models, GIS, visual analysis, and other change detection techniques. Later, İlsever (İlsever, 2012) have reduced the number of categories to four: transformation based, texture based, structure based, and pixel based. The following methods and groups are taken from İlsever (İlsever, 2012).

Pixel based is a group that consists of Image Differencing, Image Rationing, Image Regression, Change Vector Analysis, Median Filtering-Based Background Formation, and Pixelwise Fuzzy XOR Operator. The Pixelwise Fuzzy XOR Operator is not included here due to the low number of articles referring to it.

Image differencing is the subtraction of an image from one date from an image from another date of the same scene, pixel by pixel (Lu, Moran, Mausel, & Brondízio, 2004) to create a new image which contains the amount of change.

Image ratioing is to calculate the ratio between images taken at two different dates pixel by pixel, band by band, and the results should be normalized for best performance (Lu, Moran, Mausel, & Brondízio, 2004).

Image regression assumes that pixels in the first image are a linear function of the pixels in the second image. The first date image is regressed against the second image with least-squares regression to create a difference image (Singh, 1989). The difference image is subtracted from the first date image (Lu, Moran, Mausel, & Brondízio, 2004).

Change Vector Analysis is a method where the Euclidian distance between the same pixel at different times is calculated. To calculate this, two images taken at

different time are needed and two or more spectral bands from each image must be used. Each pixel will now be a vector in a multidimensional space. The two pixels with the same geographical location should share the same location in the Euclidian space if the pixels are unchanged. If a change has occurred, it is possible to detect both the magnitude of the change (distance) and the direction of the change. The magnitude of the change can be used to determine the threshold of the change, while the direction of the change can be used to classify the type of change.

Median Filtering-Based Background Formation is a method which is most used for motion detection in video that İlsever (İlsever, 2012) has utilized on satellite images. The median pixel value for each pixel is determined by sorting a timeseries of pixels, and the median pixels are used to create a new background image. The assumption is that outliers will be removed. To detect changes, other images are subtracted from the background image.

Transformation based is a group that contains Principal Component Analysis (PCA), Kauth-Thomas Transformation (KTT), Vegetation Index Differencing, Time-Dependent Vegetation Indices, and Colour Invariants. All the methods in this group transform the multispectral data to enhance some type of feature before the change between images is calculated on the transformed data. The name of the specific methods reflects the transformation of the multispectral data.

PCA reduces the dimensionality of the multispectral images to those who account for most of the variation (Singh, 1989). The principal component loadings, which indicate how much of the variance each of the variables contributes to the principal component, is then analysed to detect changes between images.

KTT is a fixed transformation of multispectral data, that redefines it into brightness, greenness, yellowness, and nonsuch values. The correlation between bands is always high within the visible bands and within the infrared bands, while the correlation between the visible and infrared bands are always low. The invariant nature of this correlation is exploited when the data is transformed. The transformed data, which enhances vegetation features, can then be used to detect changes between images.

Vegetation Index Differencing is when multispectral data is transformed into a specific index such as NDVI, where the fact that vegetation absorbs most light in the red band and reflects most light in the infrared bands. Depending on which vegetation features you want to enhance, different indexes can be calculated. The new index values are then used to detect changes between images.

Time-Dependent Vegetation Indices are vegetation indexes where the near infrared is sampled from an image with one timestamp, and red is sampled from an image with another timestamp. Furthermore, the angle of the index is calculated. İlsever decribes it as a «[…] time-dependent form of angle vegetation indices […] (İlsever, 2012). Since this index use data from two images in the calculation, the index itself describe the level of change and no further processing is needed, although thresholding could be applied.

Colour Invariants are transformations of the RGB colour space that exploit the correlations between bands in multispectral images. It was proposed for object recognition by Gevers and Smeulders (Gevers & Smeulders, 1997) and they prove that the RGB colour space can be transformed to values insensitive to object geometry, illumination direction and illumination intensity. The new values that this transformation provides, can be used to detect changes when comparing images taken at different times.

The texture based methods can use different types change detection, as shown by Tomowski et al. (Tomowski, Klonus, Ehlers, Michel, & Reinartz, 2010), but the methods are applied on texture values rather than intensity values. The two methods described by İlsever (İlsever, 2012), are Gray Level Co-occurrence Matrix (CLCM) and Entropy. Here texture values are calculated from a window around the pixels in the satellite images. The most useful texture features used in CLCM are contrast, correlation, energy, and inverse difference moment. Entropy only use entropy, which is a measure of randomness that can be used to describe texture.

Structure based methods is a group that contains Edge Detection, Gradient-Magnitude-Based Support Regions, Matched Filtering, Mean Shift Segmentation, Local Features, Graph Matching and Shadow Information. The main aspect of these methods is to identify significant structural elements in the images such as edges, shapes, or shadows, and then compare the identified structural elements between images.

It is also worth to mention that artificial intelligence also can be used for change detection, like the use of Deep Siamese Convolutional Network proposed by Yang et al. (Zhan, et al., 2017). The use of deep learning has been further tested and developed by others (Elkholy, Mostafa, ElSayad, Ebeid, & Tolba, 2023). A further review of this falls outside the scope of this thesis.

2.2. Temporal anomaly detection

Anomaly detection can be perceived as a type of target detection where you lack any information about the spectral signature of the target (Matteoli, Diani, & Corsini, 2010). Anomaly detection uses the spectral distribution of the surrounding pixels in a satellite image to detect if the *pixel under test* (PUT) has a significantly different spectral signature from its spatial surroundings (Ziemann, Simonoko, & Flynn, 2020). The application of anomaly detection could be to identify camouflaged items in a single image (Hupel & Stütz, 2022) or other objects with rare and uncommon spectral signatures relative to the background. In anomaly detection, the background is a neighbourhood of pixels surrounding the pixel under test. This neighbourhood can be the whole image or a smaller sample.

Where anomaly detection only uses a single image to find rare pixels, *Anomaly Change Detection* (ACD) use two or more images of the same scene to find pixels where the amount of change between images is larger than the normal variation between the rest of the pixels. One method is to use a change statistics image that contains statistical values that describe the changes between the images. The highest value pixels in the change statistics are the most changed pixels (Acito, Diani , Corsini, & Resta, 2017).

Temporal anomaly detection draws on the methodology of anomaly detection but changes the sampling dimension from spatial to temporal. It uses the measured spectra for the same geo-referenced pixel over time as a background rather than the surrounding pixels in the same image (Ziemann, Simonoko, & Flynn, 2020). Since it uses images taken at different times it shares some of the data quality problems with ACD.

With temporal anomaly detection one must address the problem of discerning between relevant and irrelevant anomalies. The irrelevant anomalies are those introduced to the images due to different recording conditions. This can be sensor noise, differences in contrast, brightness or focus, shadows, camera motion, atmospheric conditions and seasonal changes, or any combination of these (Acito, Diani , Corsini, & Resta, 2017).

With methods that use recordings of the same spatially co-registered pixel location with different recording dates, spatial co-registration errors could affect the performance. These small errors in geo-location introduced by the complexity of the recording system are unproblematic for many applications, but when comparing the exact same pixel position against itself an error of 1 meter at 10x10 meter resolution could affect performance. Perfect geographical correction of images from spaceborne sensors is probably impossible, and all images will contain some level of co-registration error (Acito, Diani , Corsini, & Resta, 2017). However, when using a larger number of recordings of the same pixel over time, the errors should be absorbed into the statistical model and the effect would be reduced.

2.3. RX-algorithm

In 1990 Reed and Yu (Reed & Yu, 1990) proved that their constant false rate alarm (CFAR) detection algorithm worked well on satellite images. Since then the algorithm, later known as the Reed-Xiaoli (RX) algorithm, has been widely used for anomaly detection (Manolakis, 2002), and is considered as a benchmark (Matteoli, Diani, & Corsini, 2010).

The RX-algorithm is a generalized likelihood ratio test developed for multidimensional image data. It assumes that the spectrum of the test pixel and the covariance of the background pixels is unknown. Further it assumes that the spectral information based on the background pixels fits to a multivariate normal distribution. This distribution is described with a mean vector and a covariance matrix.

The RX-algorithm calculates the Mahalanobis distance, *D*, for the pixel under test using the mean of the background pixels and the pixel under test along with the covariance matrix of the background. The distance, *D*, is then compared to a threshold (η) distance to test if the pixel under test is non-anomalous (where *D* is under the threshold distance), or if it is anomalous (where *D* is above the threshold distance).

Each multispectral pixel, $\boldsymbol{x} = \left[x_1, x_2, \dots, x_j\right]^T$, is a vector consisting of *j* bands. The background pixels, $\mathcal{B}$, can be represented as a *j* x *m* sized matrix where *m* is the number of sample pixels used to build the background model. Where each multispectral pixel is represented as a column, $\mathcal{B} = \left[\mathbf{x}_1, \mathbf{x}_2, \dots, \mathbf{x}_{m,}\right]$.

The mean of the background $\widehat{\boldsymbol{\mu}}_b$ "is given by:

$$\widehat{\boldsymbol{\mu}}_b = \frac{1}{m}\sum_{i=1}^{m} \mathbf{x}_{bi}$$

Equation 1

The covariance matrix is given by:

$$\boldsymbol{\Sigma}_b = \frac{1}{m-1}\sum_{i=1}^{m} (\mathbf{x}_{bi} - \widehat{\boldsymbol{\mu}}_b)(\mathbf{x}_{bi} - \widehat{\boldsymbol{\mu}}_b)^T$$

Equation 2

The RX-algorithm uses the covariance matrix and the mean of the background to model a multivariate normal distribution that represents the normal spectral distribution of an image, or a part of an image. This model represents the normal spectral measurements of a background, or neighbourhood. This background could

either be the whole image, or a smaller area surrounding the pixel under test, and represents the normal distribution of spectral measurements.

These differences reflect different implementations of the RX-algorithm, where the difference is the sampling method of the background pixels. The performance will differ if the background pixels are, for example, the whole image, versus a smaller area surrounding the pixel under test (Matteoli, Diani, & Corsini, 2010), (Ziemann, Simonoko, & Flynn, 2020).

The Mahalanobis distance, which the RX-algorithm below calculates, is used as a measure of how well the pixel under test, *r*, fits within the statistical model based on the background pixels.

$$D(\mathbf{r}) = (\mathbf{r} - \widehat{\boldsymbol{\mu}}_{\boldsymbol{b}})^T \boldsymbol{\Sigma}^{-1} (\mathbf{r} - \widehat{\boldsymbol{\mu}}_{\boldsymbol{b}})$$

Equation 3

When the Mahalanobis distance, *D*, increases, the likelihood of the pixel under test being a part of the dataset used to model the background decreases. The Mahalanobis distance could then be used for binary classification by using a threshold value. Distances below the threshold are non-anomalous, and distances above the threshold are anomalous (El-Rewainy & Farouk, 2011).

The squared Mahalanobis distance is likely to follow a chi-square distribution with *p* degrees of freedom (Ekiz & Ekiz, 2017). This means that chi-square can be used to set the threshold for the statistical models by using the number of spectral bands used in the experiment as degrees of freedom along with a probability level (Brereton, 2014).

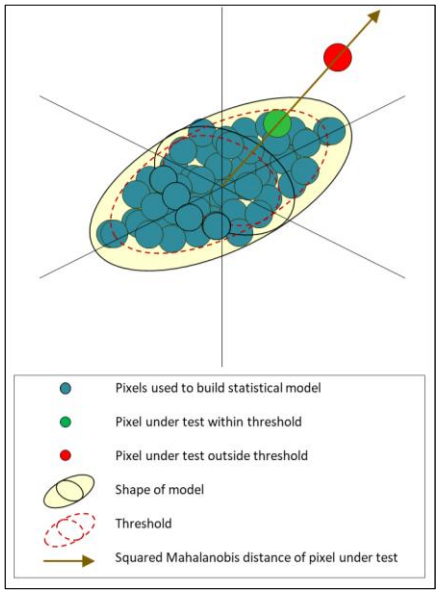

Figure 1: Illustration of a statistical model for one x, y location with sample pixels and test pixels inside and outside of threshold.

2.4. Temporal RX-algorithm

The temporal RX implementation use the same RX-algorithm, but the background pixels is not drawn from pixels spatially surrounding the pixel under test, but recordings of same geographically positioned pixel at different times. In other words, a temporal background is used rather than a spatial background. Pixels with the same *x, y* coordinates are sampled over a given time to build a statistical background model calculated with a mean and covariance matrix. This means that each pixel location

will have its own statistical model, and that the pixels under test are pixels from the same location recorded at another time than the pixels in the model.

The tests are done on pixels with the same *x, y* coordinates as its statistical model, but the test pixels are sampled from images outside the temporal background. If the distance, *D*, for the pixel under test is longer than the set threshold value, it is reasonable to assume that the pixel under test is not a part of the distribution of the temporal background. This implies that the spectral signature of that pixel is anomalous, meaning that a change likely has occurred in that location (Simonoko, Ziemann, & Flynn, 2020). This assumes that the sample pixels do not contain a larger variety of measurements; the sample pixels mostly contain one type of landcover. If the samples contain a larger portion of temporal changes like cars or boats, the model will become less capable of detecting such temporal changes. The preprocessing and selection of data for the statistical model will affect the performance of the detector. If the statistical model contains many pixels with temporary changes the model will become more generic, and it is likely that the model will become less sensitive for detection of changes.

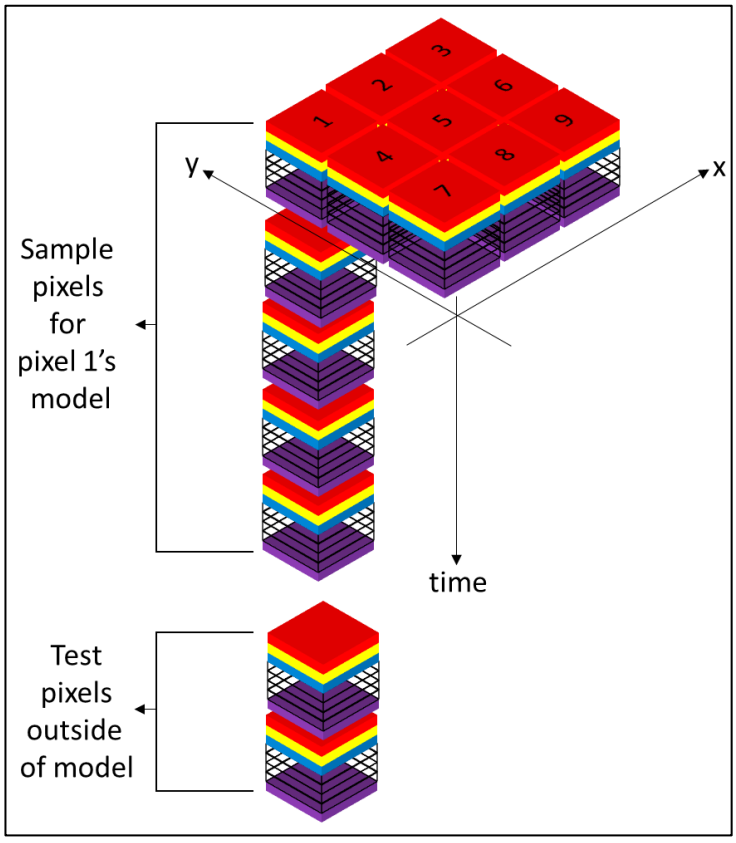

Figure 2: Illustration of temporal sampling of pixels at location 1 in a 3x3 pixel patch included in statistical model with corresponding test pixels for location 1.

Since the temporal RX-algorithm only uses one pixel as spatial resolution, it is sensitive to errors at pixel level. However, one can assume that a larger time series captures these normal errors and includes them into the background model. This would hopefully reduce the impact of such errors. Since the temporal RX-algorithm relies on the same spatial resolution as ACD, the same pixel level errors must be considered (Acito, Diani , Corsini, & Resta, 2017).

2.5. Precision, recall and F1-score

When working with classification algorithms a measure of the performance is useful for assessment. For this assignment, three metrics have been used and they are all calculated using data from confusion matrixes.

With binary classification, a confusion matrix will be a 2x2 window containing the numbers of true positives (TP), true negatives (TN), and false positives (FP) and false negatives (FN). With two classes where 0 = N (non-anomalous) and 1 = P (anomalous), the possible combinations will be TP = 1,1; TN = 0,0; FP = 0,1; FN = 1,0 where the first digit is the true class, and the second digit is the predicted class. In the tables, the correct classifications will be in the upper left and lower right corner of the table. The incorrect classifications are in the lower left and upper right corner (Tharwat, 2020).

From these numbers, different metrics can be calculated to evaluate the performance. Here recall, precision and F1-score are described.

Recall, also called hit-rate, sensitivity, or true positive rate, is a metric that compares the number of correctly classified positives with the total number of positives in the data set. The score ranges from 0, which is no recall to 1 which is perfect recall. It is calculated like this (Tharwat, 2020):

$$Recall = \frac{TP}{TP + FN}$$

Equation 4

Precision, or positive prediction value, is a metric that measures the performance of the predictions. It compares the number of correctly classified positives with the total number of predicted positives. The score ranges from 0, which is no precision to 1 which is perfect precision. It is calculated like this (Tharwat, 2020):

$$Precision = \frac{TP}{FP + TP}$$

Equation 5

F1 score, or F-measure is the harmonic mean of precision and recall. The score ranges from 0, which is low classification performance to 1 which is high classification performance. It is calculated like this (Tharwat, 2020):

$$F1 = 2 \times \frac{Precision \times Recall}{Precision + Recall}$$

Equation 6

For all these metrics, a value close to 1 indicates a better performance, and is what one should strive to achieve. Since it is difficult to eliminate all false positives and negatives, a value of 1 is hard to achieve. It is also common that when reducing one type of error, another one increases. Therefore, a compromise between precision and recall is needed. Sometimes, one type of error is preferred above the other. In such cases a deliberate decision of which type of error that should be suppressed can be made by trading recall for precision, or precision for recall. The F1 score can also

be used to find the trade-off between precision and recall, since this is their harmonic mean.

2.6. Spectral imaging

The purpose of remote sensing is to gain information about an object without coming in physical contact with the object (Manolakis, 2002). Hyperspectral imaging is a particular type of remote sensing that combines imaging and spectrometry to extract information about an object from a distance. The imaging system enables the electromagnetic information to be spatially referenced and stored as a visually interpretable image (Eismann, 2012). The spectrometer captures information about the composition of the materials measured by measuring variations of power in wavelength or frequency of light (Eismann, 2012).

Spectral images can be divided into different classes depending on the number of bands recorded simultaneously. Typically, the different types are: Panchromatic, which is one broad spectral band. Multispectral, which is several narrower bands usually between 2-10. Hyperspectral, which is many narrower bands numbering from around 10 to above 100. It is also usual to separate bands by which part of spectrum it captures.

VNIR, which is Visual and Near Infra-Red ca. 400 nm - 1000 nm wavelength.
SWIR, which is Short Wave Infra-Red ca. 1000 nm - 2500 nm wavelength.
MWIR, which is Mid Wave Infra-Red ca. 3000 nm – 5000 nm wavelength.
LWIR, which is Long Wave Infra-Red ca. 8000 nm – 14000 m wavelength.

There are no defined number of bands needed for an image to be categorized as multispectral or hyperspectral, but (Verhoeven, 2018) use these: An image containing more than red, green, and blue bands would probably be the threshold of multispectral since RGB is the normal components of a conventional colour image. The line between multispectral and hyperspectral images is also blurred, but somewhere around 10-12 bands are the normal threshold. The width of the bands is probably a better indicator since hyperspectral images usually have shorter bandwidths around 10nm and no gaps between. Multispectral images usually have bandwidths between 20 – 100nm and contain small bandwidth gaps in between bands (Eismann, 2012). The theory and methodology are common for both multi- and hyperspectral images.

The instruments used for remote sensing measures different parts of the electromagnetic spectrum. The most common part of the electromagnetic spectrum to measure within electro-optical (EO) and infrared (IR) remote sensing ranges from 400 to 14000 nm wavelength. The sensors that record these emissions are passive. That means that they mainly record light or thermal emissions in the spectrum it is designed to record, and they do not emit any own signals that returns to the sensor. Since the sensors are built for different purposes, they record different portions of the electromagnetic spectrum. These portions become the bands of the image and contains the spectral measurements in the part of the electromagnetic spectrum that the sensor is built to record (Eismann, 2012).

2.6.1. Geometric sources of error

When detecting changes at pixel level between one or more pairs of images taken at different times, it is usually assumed that the pixels are perfectly co-registered (Theiler & Wohlberg, 2012). Co-registration of satellite images is a difficult task, and

perfect co-registration is nearly impossible (Meola & Eismann, 2008). Co-registration errors have a negative effect on the performance of ACD algorithms (Meola & Eismann, 2008), (Theiler & Wohlberg, 2012) and since temporal anomaly detection use the same pixel to pixel comparison, it is reasonable to assume that large co-registration errors will affect the performance of the temporal RX-algorithm if the statistical background model do not include all the normal sources of error.

The path of the satellite is not identical between passes, and the swath of the sensor along with the shape of the earth's surface creates a need for processing of the raw image to get it georeferenced. This is done with a combination of automated and manual processes that warps the image into position (Meola & Eismann, 2008). Even if the precision is good, the errors could be at subpixel level, meaning that the co-registration errors are smaller than the spatial resolution of the images. Correcting for such small errors will influence the performance of ACD algorithms (Theiler & Wohlberg, 2012), indicating that the precision needed is high.

2.6.2. Radiometric sources of error

Spectral imaging is a complex task, and it is not straightforward to record a precise spectral signature from a distance. Both the system itself and the conditions at the time of recording affects the measurements (Eismann, 2012), but it is reasonable to assume that images from the same type of instrument have fairly consistent errors from the system itself.

How radiation transfer through the atmosphere is possible to estimate, but the complex and shifting conditions makes estimation a challenging task. Different numerical models to estimate the effect on pupil-plane measurements are used to process the raw images at the ground segment (Eismann, 2012).
The consistency of Sentinel-2 images has been tested by Doshi et al. (Doshi, Koringa, & Ghosh, 2020), and they conclude that images from the two satellites can be used interchangeably. This indicates that the quality of the image processing is good. A more detailed description of this process and a quality assessment of Sentinel-2 image processing falls outside the scope of this study.

It is relevant to consider both scattered irradiance and mixed pixels. Scattered irradiance is when objects surrounding a pixel radiates into the area of the pixel and contaminates the spectral signature of the material that the pixel actually contains (Eismann, 2012). Mixed pixels are quite common and is when the spatial resolution of the pixel is larger than the objects recorded, or when there is a clear divide inside the pixel between for instance road and grass. This means that the pixel contains more than one type of material, and the spectral signature that is recorded is a composite of the different materials represented at sub-pixel level (Manolakis, 2002). Mixed pixels could make it difficult to model a background that captures the pixel content precisely and could therefore affect the performance negatively. Due to this the temporal RX-algorithm would probably perform poorer in non-homogenous areas with large spectral variation.

Dealing with these types of anomalies are one of the most challenging problems within hyperspectral data exploitation (Manolakis, 2002).

2.7. Sentinel-2

2.7.1. Description of the mission

Sentinel-2 is a European Space Agency twin satellite mission launched in 2015 with the following objectives:

- *systematic global acquisitions of high-resolution, multispectral images allied to a high revisit frequency.*
- *continuity of multi-spectral imagery provided by the SPOT series of satellites and the USGS LANDSAT Thematic Mapper instrument.*
- *observation data for the next generation of operational products, such as land-cover maps, land-change detection maps and geophysical variables.*

(European Space Agency, 2015)

The two satellites are flying in the same polar orbit, but they are phased at 180° to optimize the revisit frequency at the Equator. The orbits are sun-synchronous, meaning that they aim to have constant angle to the sun to reduce differences in shadows and illumination recorded. The geographical coverage is between latitude 56° south and 83° north. This includes land areas and shores between Cape Horn to above Greenland, in addition to some other areas like closed seas and the Mediterranean Sea. The images recorded by both satellites are made with the Multi-Spectral-Instrument (MSI) (European Space Agency, 2015).

2.7.2. The Multi-Spectral-Instrument

The Multi-Spectral-Instrument is a passive push-broom sensor who records 13 bands. The reflected electromagnetic emissions are split onto two focal plane assemblies where one handles visible and near infrared emissions, and the other shortwave infrared. It also has a shutter mechanism that shields from direct sunlight that would contaminate the recordings.

2.7.3. Products

Sentinel-2 data exist in different processing levels. The lowest level of processing is level 0, then level 1A, 1B, 1C and finally level 2A. Level 1C and level 2A products are the two products that are released to users (Esa, 2024).

The level 1C data in this assignment contains top of atmosphere (TOA) reflectance in a fixed grid. The spatial reference system is a combined UTM projection and WGS84 geodetic system (European Space Agency, 2015).

The images are radiometrically and geometrically corrected, and they are delivered in 100km^2 tile sets. Each tile corresponds to a grid in the Sentinel-2 level 1C tiling grid that gives 100km^2 square a unique name.

2.7.4. Temporal and radiometric resolution

The revisit frequency at the equator of one Sentinel-2 satellite is 10 days, and the constellation of the two satellites reduces the temporal resolution to 5 days (European Space Agency, 2015).

The radiometric resolution is a measure of how many unique values the sensor can record. A higher number means that the instrument should be more capable of detecting accurate differences in intensity or reflectance. It is expressed as a bit-number, and for Sentinel-2 that is 12-bits. This means that the measurements can range from a value of 0 to 4095.

2.7.5. Spatial and spectral resolution

The Sentinel-2 products have 13 different spectral bands, which vary in spatial resolution between 10-, 20- and 60-meters. It delivers data in four 10-meter bands, six 20-meter bands and three 60-meter bands. *Figure 3*, below, displays all bands in all spatial resolutions with the respective spectral resolutions.

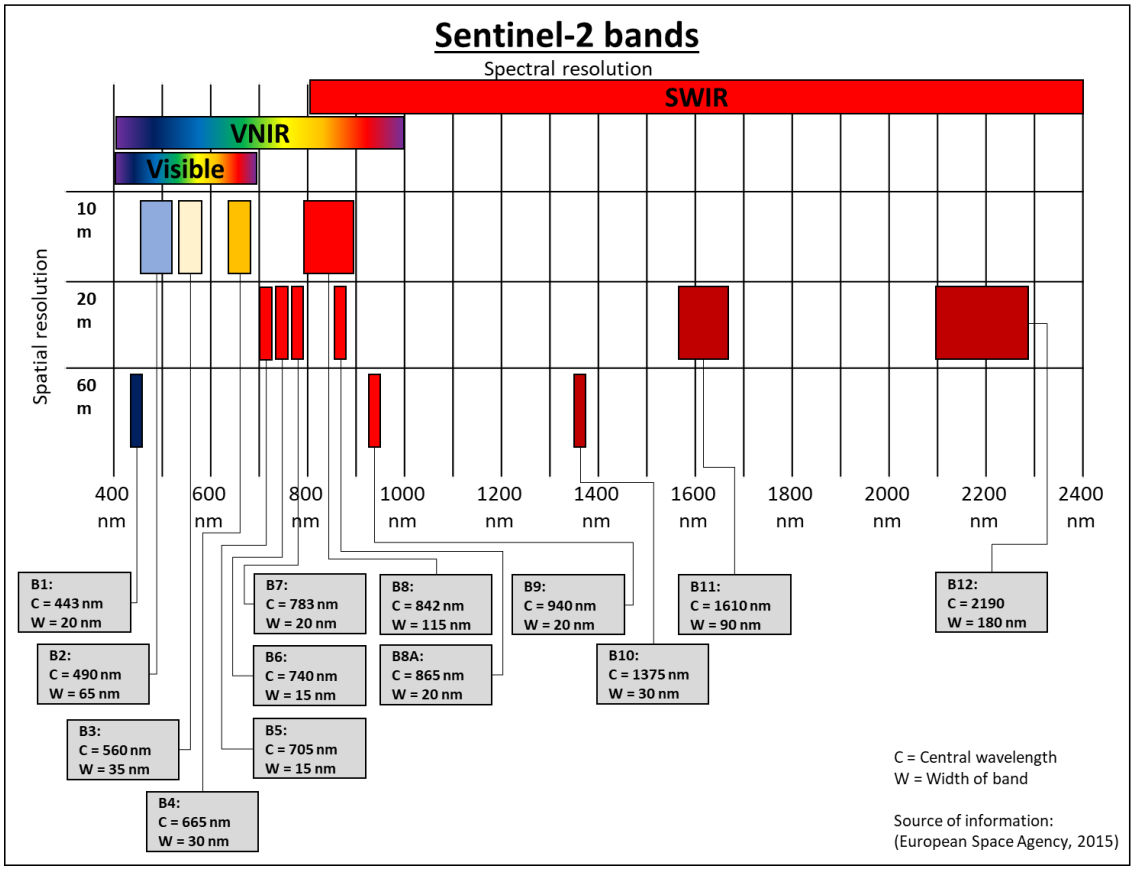

Figure 3: Sentinel-2 bands spatial and spectral resolution (European Space Agency, 2015).

Page intentionally left blank

3. Methodology

First the study area was selected, and relevant patches was identified. Then all the Sentinel-2 images were cropped to the study area. After that the images were visually inspected. Many of the images where either empty or contained heavy clouds or snow. Such images would introduce known errors into the statistical background that we use to model the original state for the pixel location, or they would create false positives for the pixel under test. Since the data do not contain measurements of what we are studying, but measurements of a phenomena that obscures the recording of the ground, they are removed. Of the 303 images, 233 were manually inspected and excluded, leaving 70 good images.

Now a sequence of visual inspections of was conducted by iterating through all the remaining 70 RGB-images to visually classify the study area pixels as changed or unchanged. If the pixel did not appear to have changed, it was assigned the number 0, and if it did contain an apparent change the number 1 was assigned. This binary classification is used as the ground truth, which is how a human would classify locations tested.

The Sentinel-2 images are now ready to be classified with the temporal RX-algorithm and compared to the human assessed binary classification data. The temporal RX-algorithm was configured to work through each of the 9 pixels in all the 5 patches, a total of 45 spatial pixel locations.

In this process the temporal RX-algorithm calculated a statistical background with the first 20 pixels and then tested the remaining 50 pixels sequentially as pixel under test to evaluate if it is likely that it is a part of the statistical background or not. If the Mahalanobis distance of the pixel under test was longer than the threshold, the pixel under test was classified as outside the background model, implying a change. These changed pixels were given the value 1, while those with a distance shorter than the threshold was given the value 0. After one pixel location was evaluated, a new background was modelled for the next pixel location and the pixels under test were evaluated against the new background model.

The binary classification data created by the temporal RX-algorithm was then compared to the human made classification data to compare the performance of the temporal RX-algorithm against the performance of the human. This data was then used to create different plots and figures.

The study was conducted in MATLAB 2022b, and several scripts were written for the different parts.

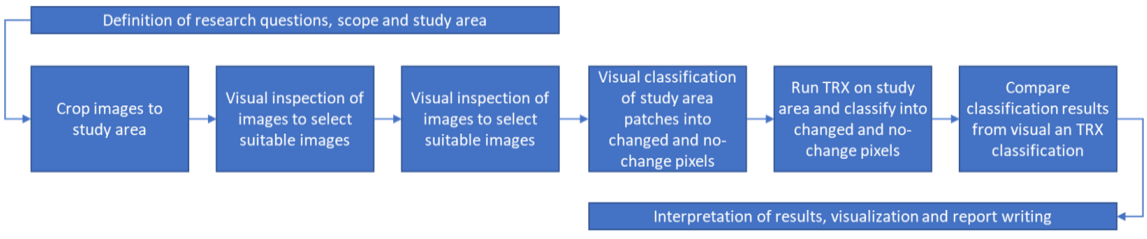

Figure 4: Flowchart of the steps in the study

3.1. Study area and patch selection

The study area is called Hennøy and is a small peninsula approximately 20 km north of Florø in the western part of Norway. The area is quite diverse, and contains both water, windmills under construction, and different types of vegetation and

infrastructure. At Hennøy, five 3x3 pixel patches with interesting features within the area was located using internet sources.

Patch 1: 61.7839°, 5.1327°
Patch 2: 61.7963°, 5.1454°
Patch 3: 61.7777°, 5.1565°
Patch 4: 61.7655°, 5.1374°
Patch 5: 61.7715°, 5.1600°

The position close to the shore is chosen because the general climate is assumed to reduce the number of days with snow. This allows Sentinel-2 imagery over a northern area to be used without discarding too many images due to snow. The position also introduces water with a harbour into the images, which is an interesting area to study temporary changes. It was also selected because it has been built windmills in the area after 2015. The Norwegian Water Resources and Energy Directorate online maps containing wind power were used to identify areas with recent windmill construction (NVE, 2022). In addition, the topography is not flat, and the area contains built-up areas and nature. The area is completely within the Sentinel-2 1C 32VKP tile.

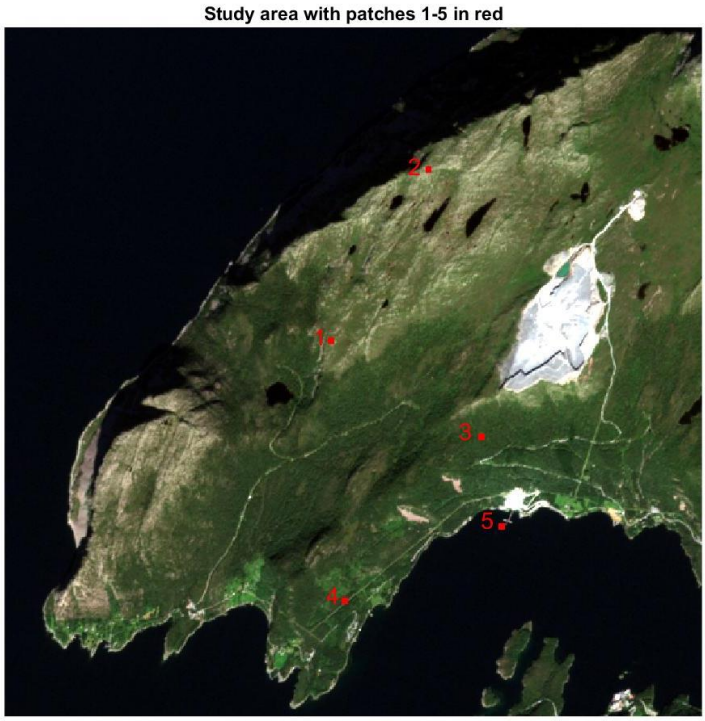

Figure 5: Image of study area with patch positions.

3.1.1. Patch 1 – Windmill construction, border

This patch was selected because it contains an emerging windmill. The 3x3 pixel patch is deliberately placed at the border of the construction to introduce challenges with sub-pixel changes and potential co-registration errors. The patch starts as an area with natural vegetation in 2015 and ends in 2017 with a road containing a fundament and a windmill in the eastern part, and natural vegetation in the western part.

Figure 6: Before, under and after image of patch 1. Image number (YYYYMMDD): 2 (20150818), 30 (20190412) and 69 (20211104).

3.1.2. Patch 2 – Windmill construction, centre

This patch was selected because it also contains an emerging windmill, but the 3x3 pixel patch is deliberately placed centred on the final windmill. It is done to reduce the probability of having pixels containing both forest and construction work at the same time. The patch starts as an area with natural vegetation in 2015 and ends in 2017 with a road containing a fundament and a windmill in the centre of the patch.

Figure 7: Before, under and after image of patch 2. Image number (YYYYMMDD): 2 (20150818), 30 (20190412) and 69 (20211104).

3.1.3. Patch 3 – Unchanged Forest

This patch is chosen because it does not contain any known or identifiable changes except one slightly cloudy image (nr.70) and is included as a reference area. The patch starts as an area with natural vegetation and ends as an area with natural vegetation.

Figure on next page.

Figure 8: Before, under and after image of patch 3. Image number (YYYYMMDD): 2 (20150818), 30 (20190412) and 69 (20211104).

3.1.4. Patch 4 – Removal of vegetation

This patch was selected because it also contains man made changes, but it is not identified that unnatural materials are introduced into the area, as with the windmills. The changes are also appearing later in the time series than the windmill construction and gives a different temporal distribution of changes. The patch starts as an area with natural vegetation, forest, and grass, and ends with bare soil.

Figure 9: Before, under and after image of patch 4. Image number (YYYYMMDD): 2 (20150818), 30 (20190412) and 69 (20211104).

3.1.5. Patch 5 – Harbour

This patch was selected because it does not contain vegetation. It contains temporary changes in the form of boats arriving and departing, in contrast to the other patches where the areas are permanently changed. The 3x3 pixel patch is deliberately placed on the biggest boats, but since the boats often are smaller than the patch, sub-pixel anomalies and potential co-registration errors could be introduced. The patch starts as an area with water and ends as an area with water. In between several boats has visited the harbour.

Figure on next page.

Figure 10: Before, under and after image of patch 5 with temporary change. Image number (YYYYMMDD): 2 (20150818), 30 (20190412) and 69 (20211104).

3.2. Data and band selection

The raw data for this thesis is a time series of 303 level 1C Sentinel-2 SAFE folders with images of the Sentinel-2 1C tile grid 32VKP. The first image is dated 25.07.2015 and the last 04.11.2022. The tile was cropped into a smaller study area according to the flowchart (Figure 11). In the experiment only 11 of the 13 bands where used. Band 9 and 10, Water Vapour and SWIR cirrus, where excluded just as Ziemann et al. (2020) did when they first used the RX-algorithm on temporal data.

The tested pixels have a 10x10 meter spatial resolution, but the data used have 10-, 20- and 60-meter resolution. To handle this, a nearest neighbour resampling was used to retrieve measurements from the 20-, and 60-meter bands.

Figure on next page.

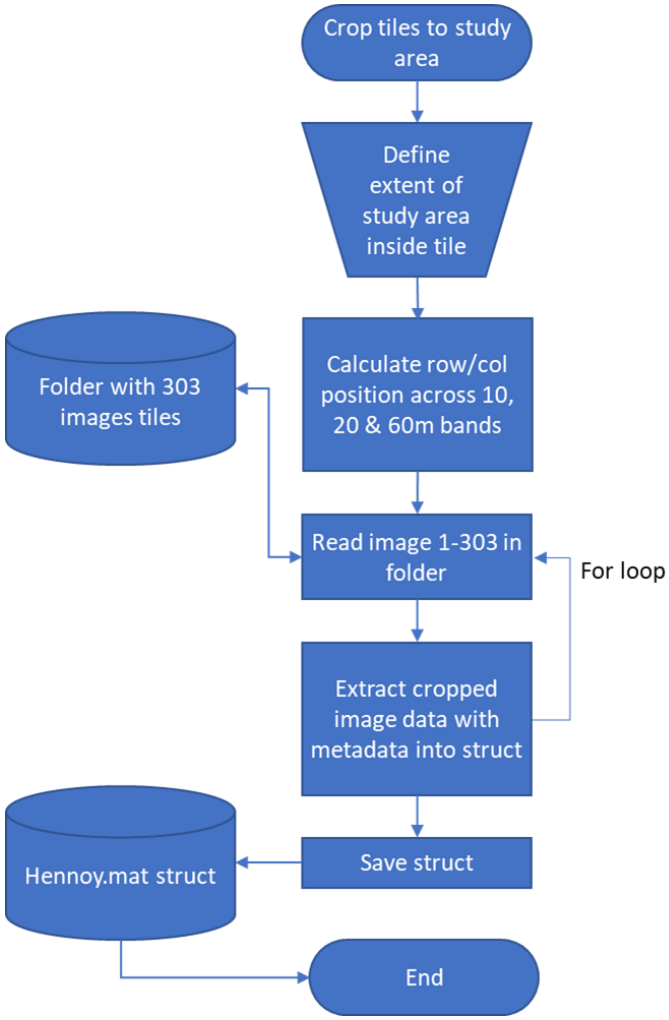

Figure 11: Flowchart describing Sentinel-2 cropping process.

3.3. Quality inspection and image selection

When visually inspecting the data, many of the images happened to be unsuitable. Some of them where empty, while others contained heavy clouds or snow. Empty images and images containing snow and significant clouds were removed from the dataset used for the study to ensure that the statistical background being modelled contains actual ground measurements. This reduces the risk of the models becoming too general to represent the ground, and that the pixel under test would not obviously contain a measurement of something else than the ground, resulting in false positives. After removing the 233 images that was judged unsuitable, the final dataset contained 70 images.

An automated approach to discarding images with low quality and unwanted features is the most elegant method, but it also reduces the control over the experiment and increases complexity. To have full control over the images used as training data, and to ensure that images that obviously would create false alarms where excluded, a list of visually inspected and approved images was created. The images in the final list include a few with clouds and shadows but excludes the most of them. In the first 20 images boats in the harbour are also excluded to ensure that the background models do not include anomalies that we want the algorithm to detect. The quality inspection was a machine-aided process with a Matlab script that is illustrated in the flowchart in *figure 12*.

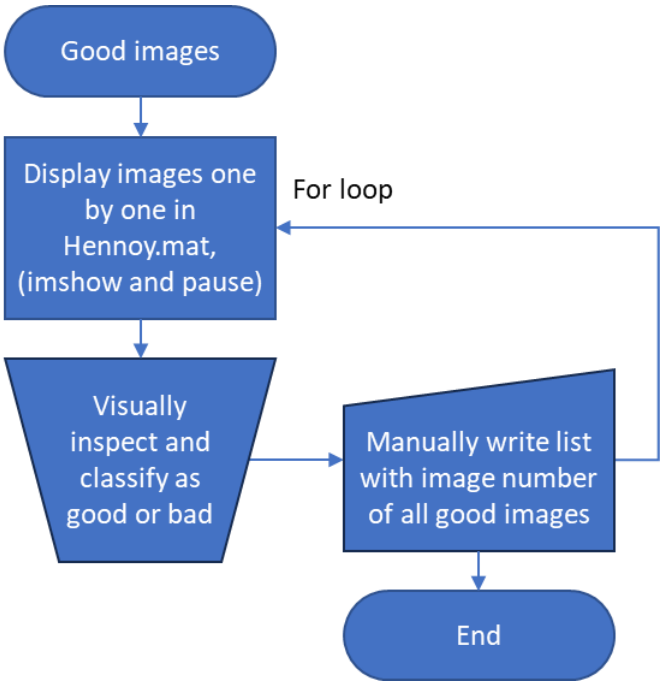

Figure 12: Flowchart describing the quality inspection process.

3.4. Ground truth

To assess the performance of the temporal RX-algorithm a ground truth was made to compare the classification made with the temporal RX-algorithm versus the classification made by a visual inspection of the images. A precise visually classification and annotate of images with 10x10 meter resolution is difficult. Objects smaller than 10x10 meters could hide inside the pixels, but the visual ground truth is done with the same data that the automated process uses.

The ground truth was established manually by visually inspecting each pixel in each patch in all the images. Each pixel was visually inspected at different zoom levels to enable the best interpretation of the pixel. If the pixel was assessed to contain something different than the original state, the pixel was flagged as changed with the value 1, and if it contained the same as the original state it was flagged with the value 0. The ground truth values were stored in a matrix compatible with the structure of the output analysis data from the temporal RX-algorithm. A table with the binary classifications, 0 and 1, was the result from this process. It was aided by a script that displayed each pixel inside a red line with surrounding areas at different zoom-levels illustrated in the flowchart, *figure 1*3.

Figure on next page.

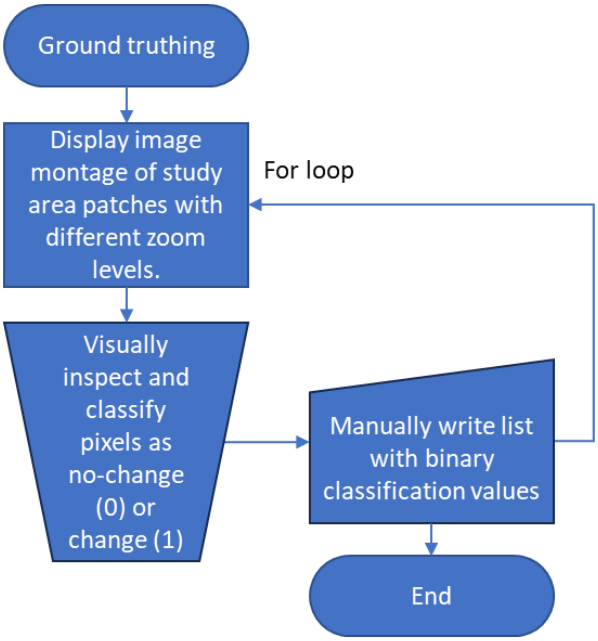

Figure 13: Flowchart describing the ground truthing process.

3.5. Experiment description

The experiment was conducted by using the satellite images in the time series which are older than the construction work to model the background for the temporal RX-algorithm´s covariance matrix and background mean. Black images, images with heavy clouds and snow were manually removed before the experiment was conducted. From the remaining images, the statistical background was drawn from the first 20 images. 20 images were a reasonable limit to have a small gap in time between the statistical model and the first signs of construction. The final dataset contained 20 images which was used to model the backgrounds for the pixel locations, and 50 images to draw test pixels from.

The experiment iterated through each pixel of all the patches sequentially. The temporal RX-algorithm was applied like this on one pixel before it moved to the next pixel where the same procedure was applied.

First the background pixels were drawn from the 20 first images for a *x*, *y* coordinate, and the mean and covariance matrix were calculated. Then the pixel under test was drawn from a later image with the same *x*, *y* coordinates as the background pixels. The algorithm worked in depth of time with the spatial distribution of one pixel where each pixel under test was drawn from image 21 to 70. The squared Mahalanobis distance for the pixel under test, which equals to the squared RX-score, and the threshold was used to test the hypothesis.

To find the threshold value, 11 degrees of freedom was used, corresponding to the number of spectral bands used in the experiment, and the *p-value* was set to 0.05. This gives a threshold value of 19.67 (Brereton, 2014). The following hypothesis was used to determine if the pixel under test was a part of the statistical model or not:

$$H_0 = \sqrt{D} \geq 19.67 = \text{unchanged}$$

$$H_1 = \sqrt{D} < 19.67 = \text{changed}$$

Unchanged pixels were given the classification number 0 and changed pixels 1. This gave a 1x50 matrix with ones and zeros which was concatenated with the corresponding matrix from the ground truthing process. This 2x50 matrix were used to calculate the number of true positives, true negatives, and false positives and false negatives.

The squared Mahalanobis distances for all the classified pixels in the same location were plotted against the corresponding image number. In the bottom of these plots the threshold value is displayed as a straight line. According to the classification produced, a colour was given to the bar chart. This plot shows when in time, by image number in the time series, the anomalous changes were introduced. This ends the process for one pixel.

The same procedure was done for each pixel in every patch, starting with the creation of a new background model from the 20 first images, then testing the pixels under test, comparing the classification with the ground truth, and plotting the results.

The script worked its way through all the 9 pixels in a patch before the concatenated matrixes with ground truth and predicted values was used to calculate a spatial confusion matrix and a combined confusion matrix for the first patch.
The spatial confusion matrix keeps the spatial distribution of true positives and negatives, and false positives and negatives of the pixels within each patch, while the combined confusion matrix sums up the total number for all nine pixel positions in the patch. The following four patches were analysed the same way.

In the end, a confusion matrix with the total number of true positives, true negatives, and false positives and false negatives was generated from all the 2x50 matrixes for the total number of pixels. The flowchart in *figure 14* depicts how the script worked in this step.

Figure on next page.

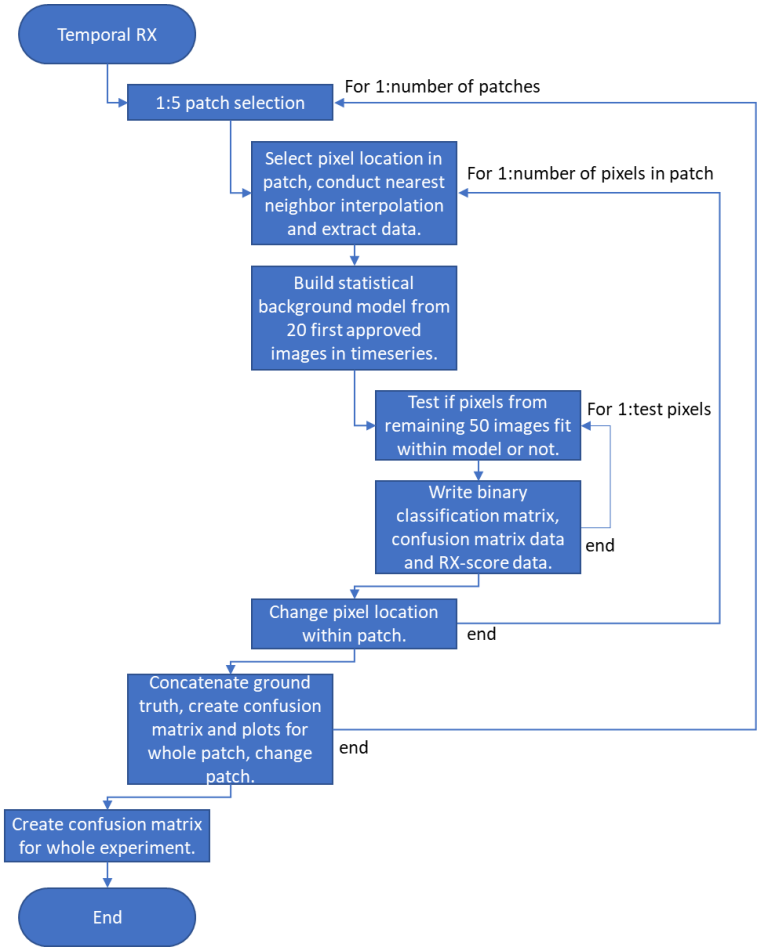

Figure 14: Flowchart describing the temporal RX-algorithm image classification process.

4. Results

For each patch a figure is provided. It contains a bar chart displaying the squared RX-score for each pixel over time where image number (21-70) for pixel under test is shown. The bar chart is colour coded according to if it is a true positive, true negative or false positive or false negative. The setup follows the *x, y* location of each pixel within the patch. This means that the upper left bar chart corresponds to the upper left pixel in the patch (pixel 1), and this again corresponds to the location in the spatial confusion matrix.

The spatial confusion matrix, which is a heatmap that displays the spatial distribution of TP, TN, FP and FN for the whole patch where each of the 4 classes has its own 3x3 pixel window. This gives a total of four 3x3 windows, where upper left is TN, upper right is FP, lower left is FN and lower right is TP. This makes it possible to study the spatial distribution of errors inside each patch.

In addition, there is a normal confusion matrix with 4 windows where each window contains the total of TP, TN, FP and FN in both numbers and percent for the whole 9-pixel patch.

4.1. Patch 1 - Windmill construction, border

When studying *figure 15*, the first temporal RX-algorithm detected anomalies appears in image 24, which are false positives. The first true positives appear in image 25, and this corresponds well with the visual signs of construction inside the patch. From image 24 to 70, the anomaly score changes significantly both between pixels and within pixels. Some of the values are above and some are below the threshold. This is expected since the patch contains both changed, pixel 6 and 9, and unchanged pixels, 6 and 9. When inspecting *figure 16*, the other pixels seem to be either mixed or shift over time. However, highest density of true negatives follows the left side of the patch, that corresponds with low level of change. The highest density of true positives is in the lower right corner, that covers the centre of the construction. The misclassifications seem to be overrepresented along the border between changed and unchanged pixels.

Figure on next page.

Figure 15: Patch 1 plots

The patch border, red line in *figure 16*, seems to shift slightly over time, containing an increasing, decreasing and then increasing part of the construction site that is visually detectable. If you compare image 28 and 32, image 38 and 40, image 46 and 47, and image 55 and 56 this phenomenon is present. This shift is most present in the east/west direction since the patch is more centred on the construction site in

the north/south direction. This could happen because of co-registration errors or differences in light conditions/shadows, or in the later ones in the time series, by the rotation of the windmill blade. When comparing this with the spatial confusion matrix, most true negatives are located in the western part of the patch, and most true positives are located in the eastern part of the patch.

With 8.4% false negatives and 9.8% false positives, the performance of the temporal RX-algorithm is poorer on this patch than the overall performance for the experiment. This underperformance is distributed along the outer border of the construction site.

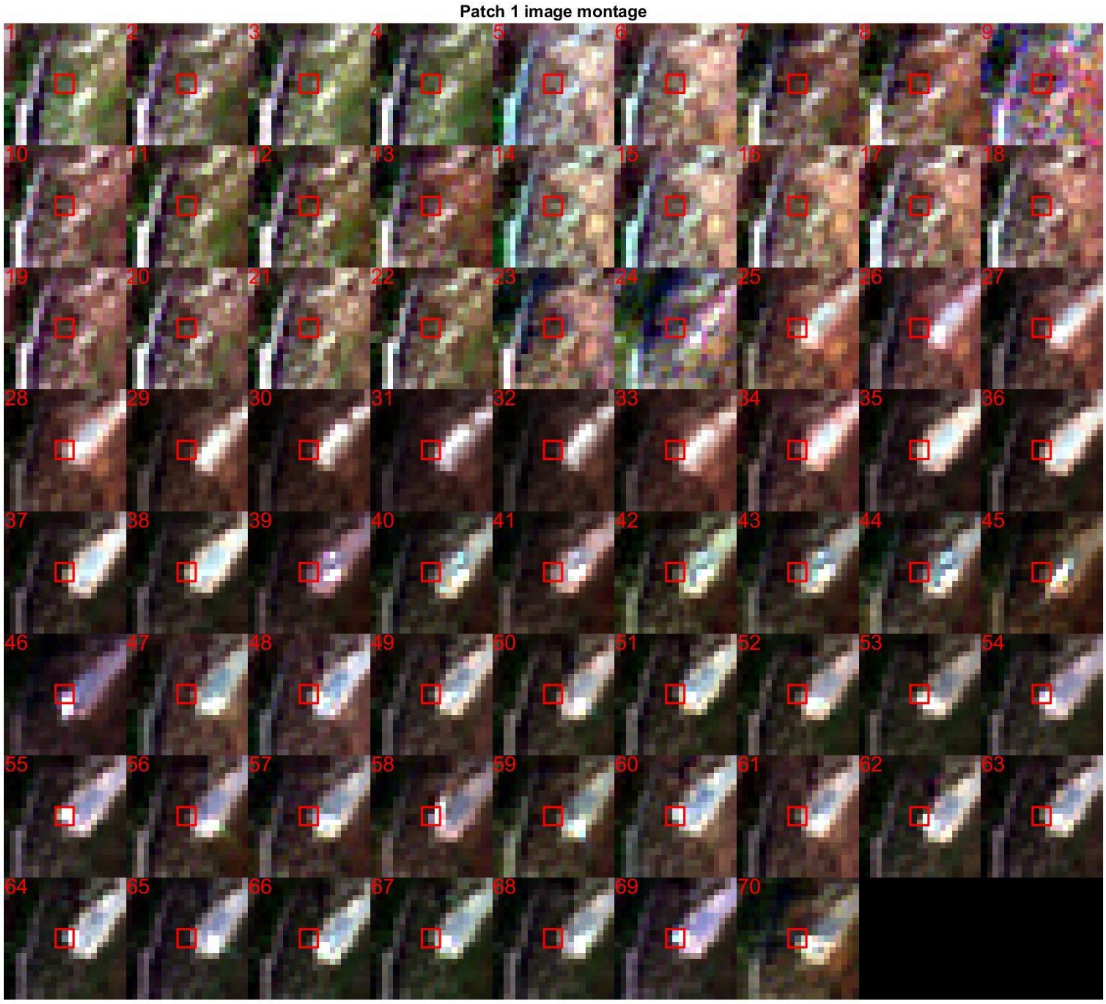

Figure 16: Patch 1 highlighted in red, background data = image 1-20, test data = image 21-70.

4.2. Patch 2 - Windmill construction, centre

When studying *figure 17*, the first temporal RX-algorithm detected anomalies appears in image 23, which are likely false positives. From image 24 onwards anomalies are detected, and they coincide with the first verifiable visual signs of windmill construction. From image 23 to 70, the anomaly score is constantly high, and the few non-anomalous pixels are found in image 21 and 22 which is before the construction. The anomaly score is consistent with a patch where many pixels are permanently changed from one state to another, where the new state is different than the state modelled by the statistical background.

Figure on next page.

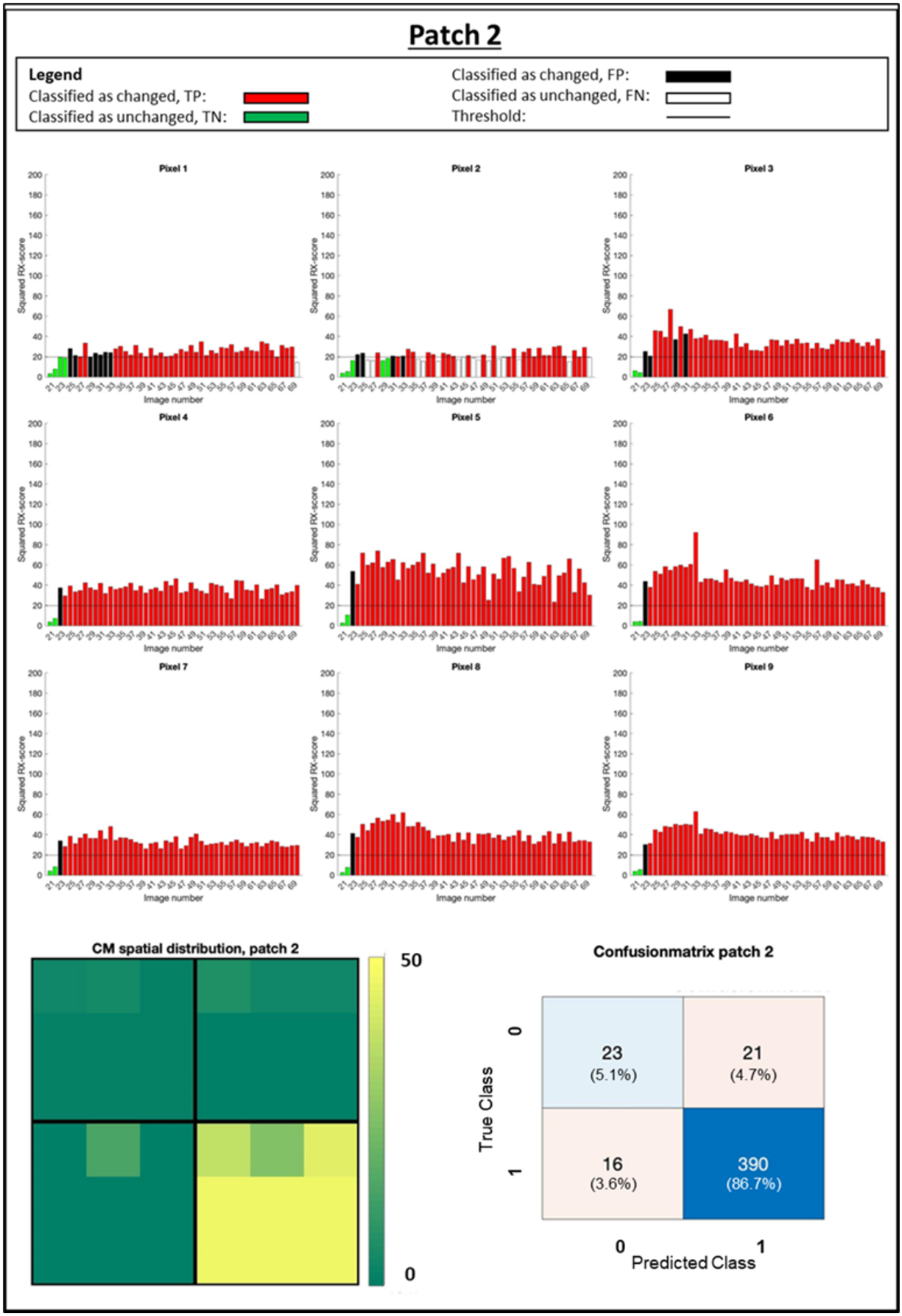

Figure 17: Patch 2 plots

The contents within the patch border, red line in *figure 18*, could seem to shift slightly, but the patch contains a part of the construction site quite constantly with a border to natural vegetation in the north/top. The blade of the windmill, which is introduced in image 39, creates some of the shifts in shape in this patch. This makes it harder to visually determine if the patch is stable or if it, like patch 1, seems to have some co-registration errors.

The spatial confusion matrix shows that the temporal RX-algorithm has a lower performance in the northern/upper part of the 3x3 patch with some false positives and false negatives. This is shown at the upper row of pixels in the spatial confusion matrix.

With 3.6% false negatives and 4.7% false positives, the performance of the temporal RX-algorithm is approximately as good as the overall performance for the experiment.

Figure 18: Patch 2 highlighted in red, background data = image 1-20, test data = image 21-70.

4.3. Patch 3 - Unchanged Forest

When studying *figure 19*, the first temporal RX-algorithm detected anomalies appears in image 57 and is an error which coincides with some false positives in patch 4 and 5 and cannot be explained well. The second detected anomaly is in image 70 where it correctly classifies clouds as anomalous. The low number of anomalies is consistent with a patch where the tested pixels are not different than those in the statistical background of the location.

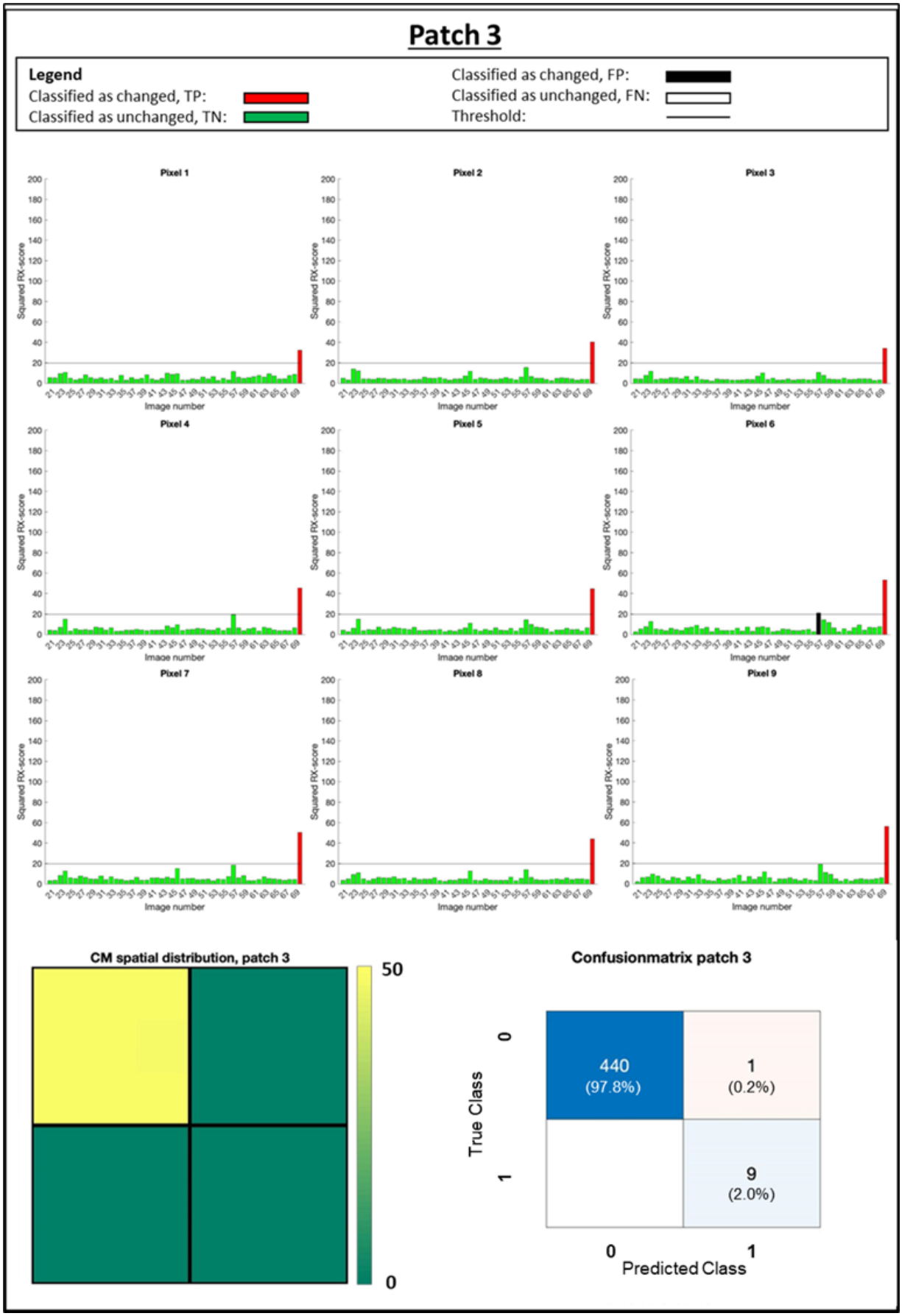

Figure 19: Patch 3 plots

It is not possible to detect if the quality of the co-registration by inspecting the pixels within the patch border, red line in *figure 20*, since the natural vegetation fills the whole patch quite constantly.

With 0.0% false negatives and 0.2% false positives, the performance of the temporal RX-algorithm is better on this patch than the overall performance for the experiment.

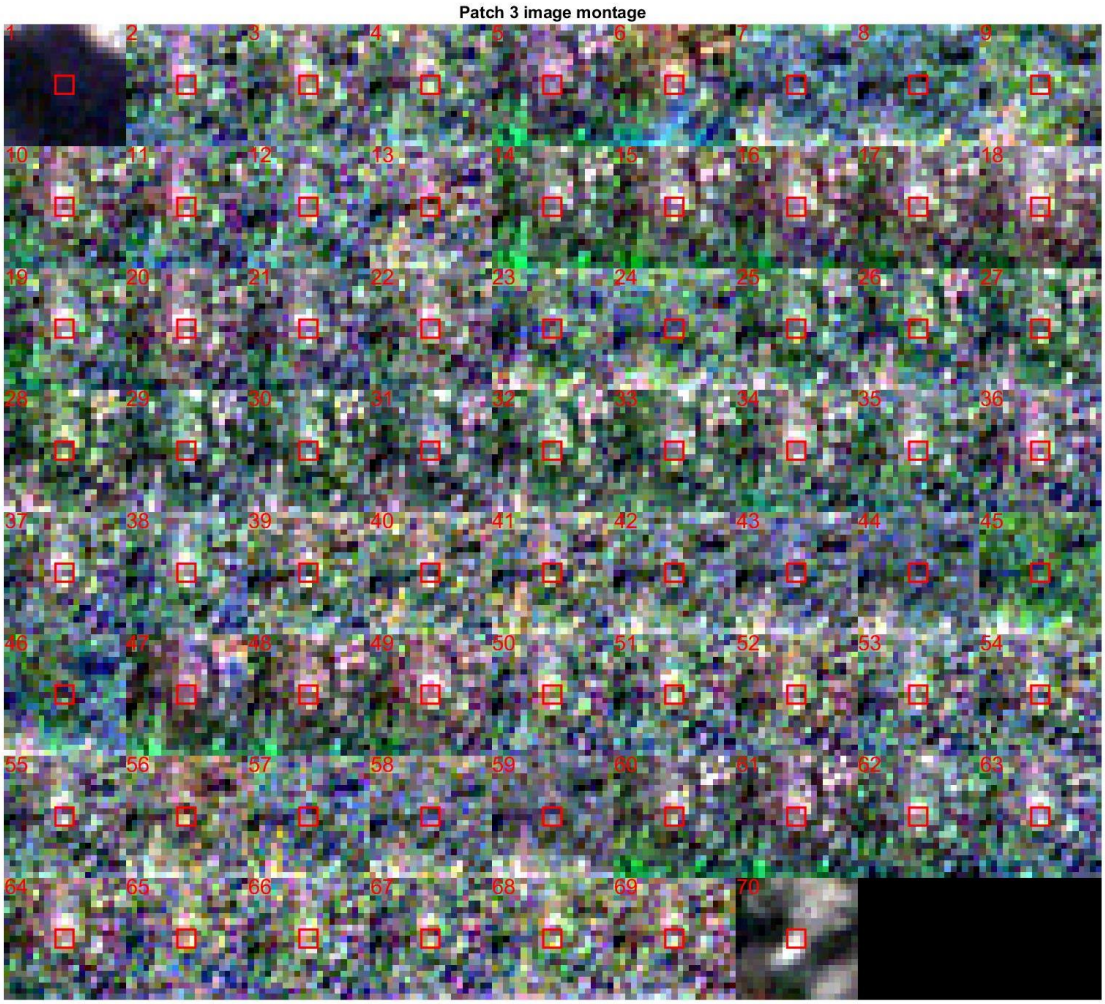

Figure 20: Patch 3 highlighted in red, background data = image 1-20, test data = image 21-70.

4.4. Patch 4 - Removal of vegetation

When studying *figure 21,* the first temporal RX-algorithm detected anomalies appears in image 24, then 45, 46, 57 and 59. These are likely false positives, and some of them appear at the same time as false positives in other patches due to a phenomenon that gives the whole RGB-image a greenish hue.

Then it detects parts of the true changes from image 60. Along with the correctly classified changes, it produces quite some false negatives along the centre diagonal along pixel 3, 5 and 7 visible in *figure 21,* but the general anomaly score is kept high for the rest of the time series.

It is difficult to determine if there are any co-registration errors since there are no reference point other than the diagonal terrain feature that runs like a line thru *figure 22*. This means that a 1-pixel shift both up and right, or down and left is difficult to detect when visually inspecting *figure 22*; an equal shift in both the *x* and *y* direction would maintain a similar intersection with the patch border, red line. However, it seems like the white detail in the lower right corner of the image bounces around. This indicates that the co-registration is not perfect. The best illustration of this is between image 61 and 62 where the content within the patch also changes slightly.

Figure on next page.

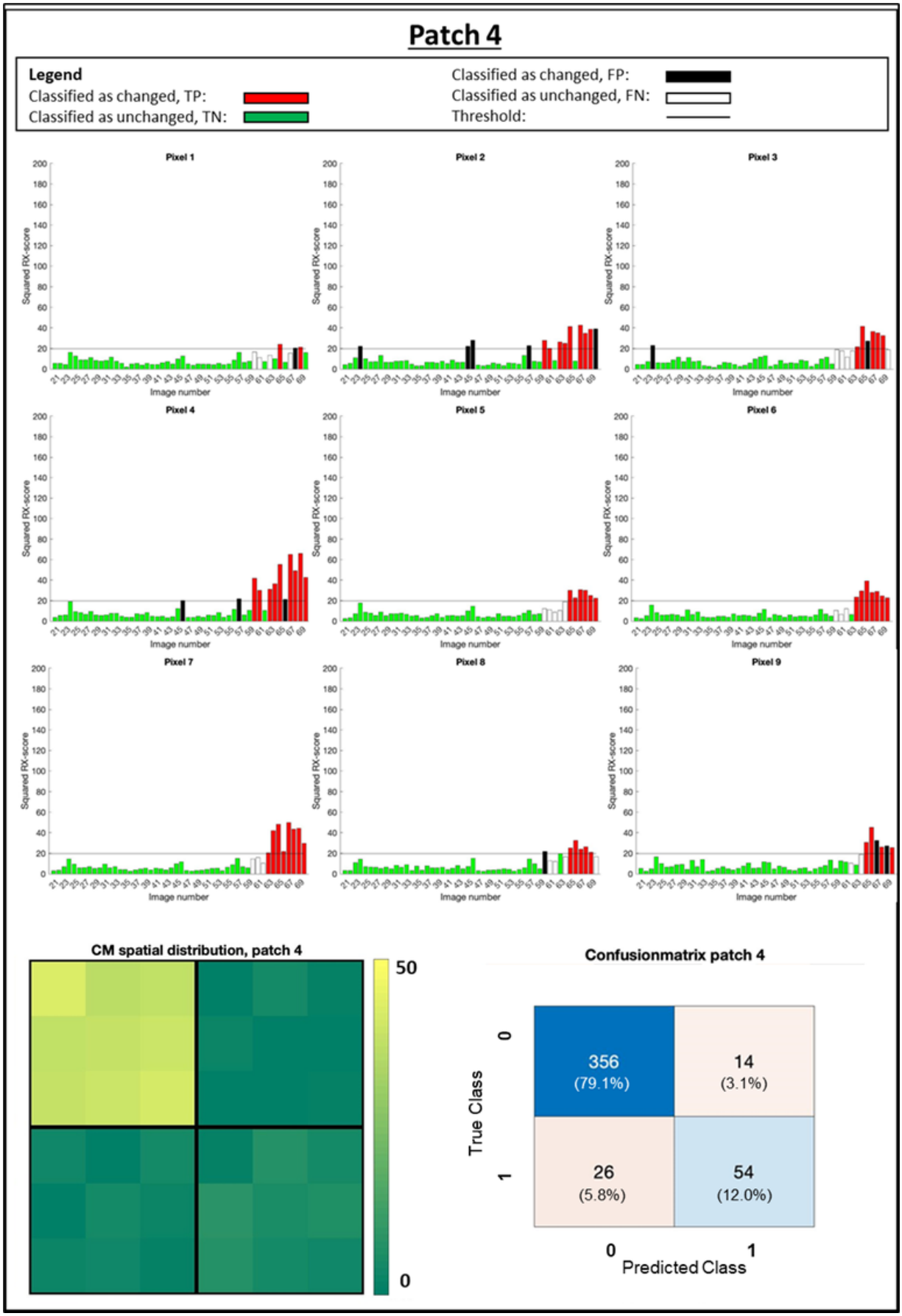

Figure 21: Patch 4 plots

The spatial confusion matrix in *figure 21* shows that the temporal RX-algorithm has a lower performance with more false positives on both sides of the road/strip of bare soil. Most of these false positives are located in pixel 2 and 4, and falls just outside the diagonal line that runs thru pixel 3, 5 and 7. The false negatives are clustered along this diagonal strip of bare soil.

Scattered irradiance from the surrounding trees is a potential explanation since the shadows in the images in *figure 22* indicates high trees along the strip of bare soil. A higher presence of spectral values from vegetation transferred into pixels with soil could possibly mask the soil and emulate vegetation. Especially since the algorithm use several infrared bands that the visual interpretation does not use.

Another explanation is that the classification made by a human is worse than the automated classification. In this patch it is difficult to determine exactly when the changes start.

With 5.8% false negatives and 3.1% false positives, the performance of the temporal RX-algorithm´s false positive performance is better, and the false negative performance is worse on this patch than the overall performance for the experiment.

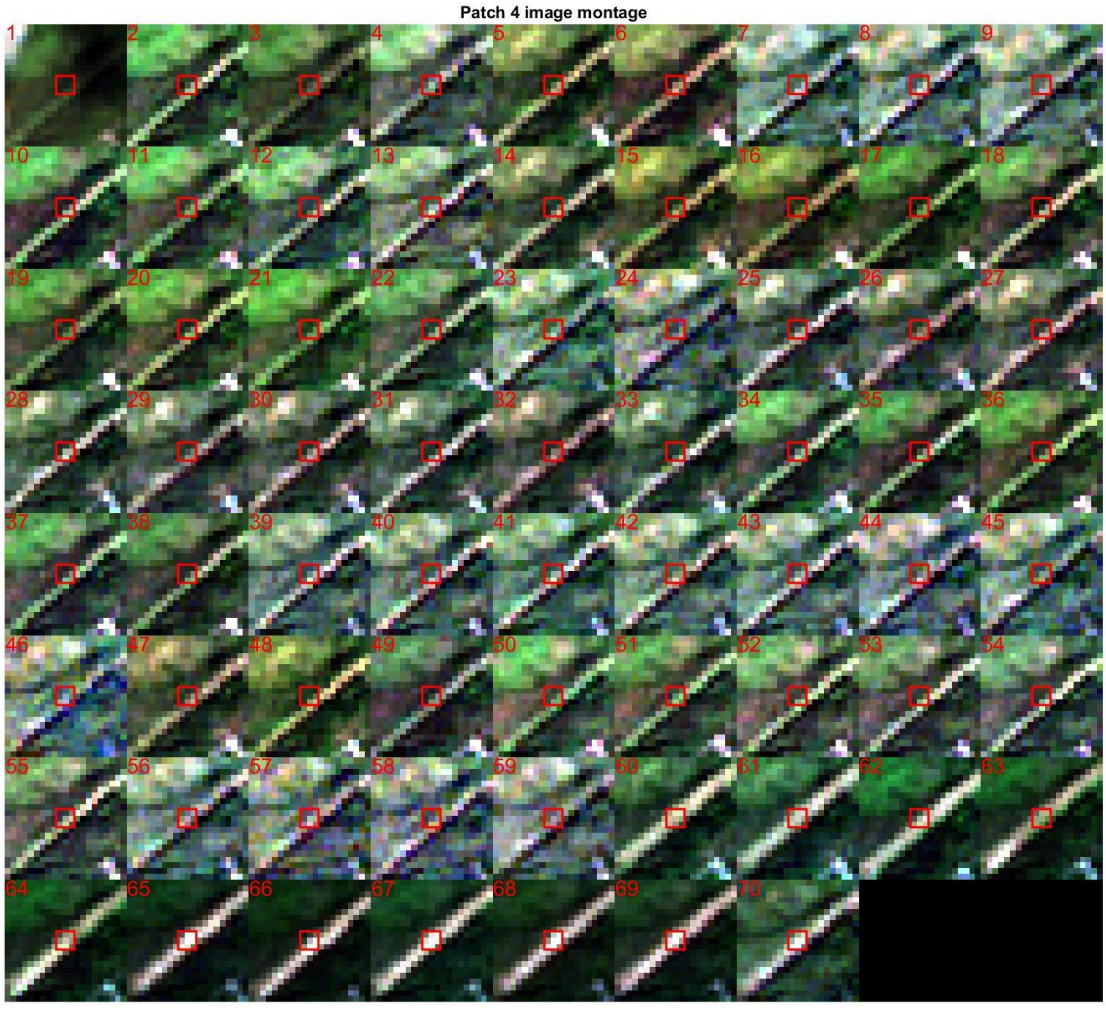

Figure 22: Patch 4 highlighted in red, background data = image 1-20, test data = image 21-70.

4.5. Patch 5 – Harbour

The temporal RX-algorithm detected anomalies in this patch are distributed between boats, clouds, and false alarms. When studying *figure 23*, the false alarms that do not contain a boat in the image are 22, 56 and 57. The rest of the false positives are in images with boats, but where the human has classified the pixel as water next to the hull of the boat, rather than a boat. The problem here is to decide where to draw the line between boat and water. In this case the human has been more inclined to classify the border pixels as water, and the RX-algorithm more inclined to classify it as a boat.

The boats are correctly detected as anomalies in image 30, 34, 36, 37, 38, 39, 50, 52, 54, 63 and 67. The temporal RX-algorithm can detect temporary changes where an object is introduced into a test pixel for a limited time, when the modelled background does not contain such objects.

Figure on next page.

Figure 23: Patch 5 plots

For this patch, co-registration cannot be evaluated by studying *figure 24*, since the only reference point seems to be moving. The position of the harbour in image 3 and 4 has shifted significantly counterclockwise, and this indicates that the installation is floating or movable. It is also worth noting that image 24 have a distinctly different colour than the rest. The reason for this discolouration of the water cannot be determined precisely.

In general, the boats in these images are docked across the patch with the line between the boat and water in the bottom of the patch. The false positives are present at the bottom of the patch, shown with lighter green squares in the upper right window of the spatial confusion matrix at pixel position 7, 8 and 9. The higher presence of false positives at left side could be explained with the slight clockwise rotation of the boats.

With 0.0% false negatives and 4.7% false positives, the performance of the temporal RX-algorithm is better on this patch than the overall performance for the experiment.

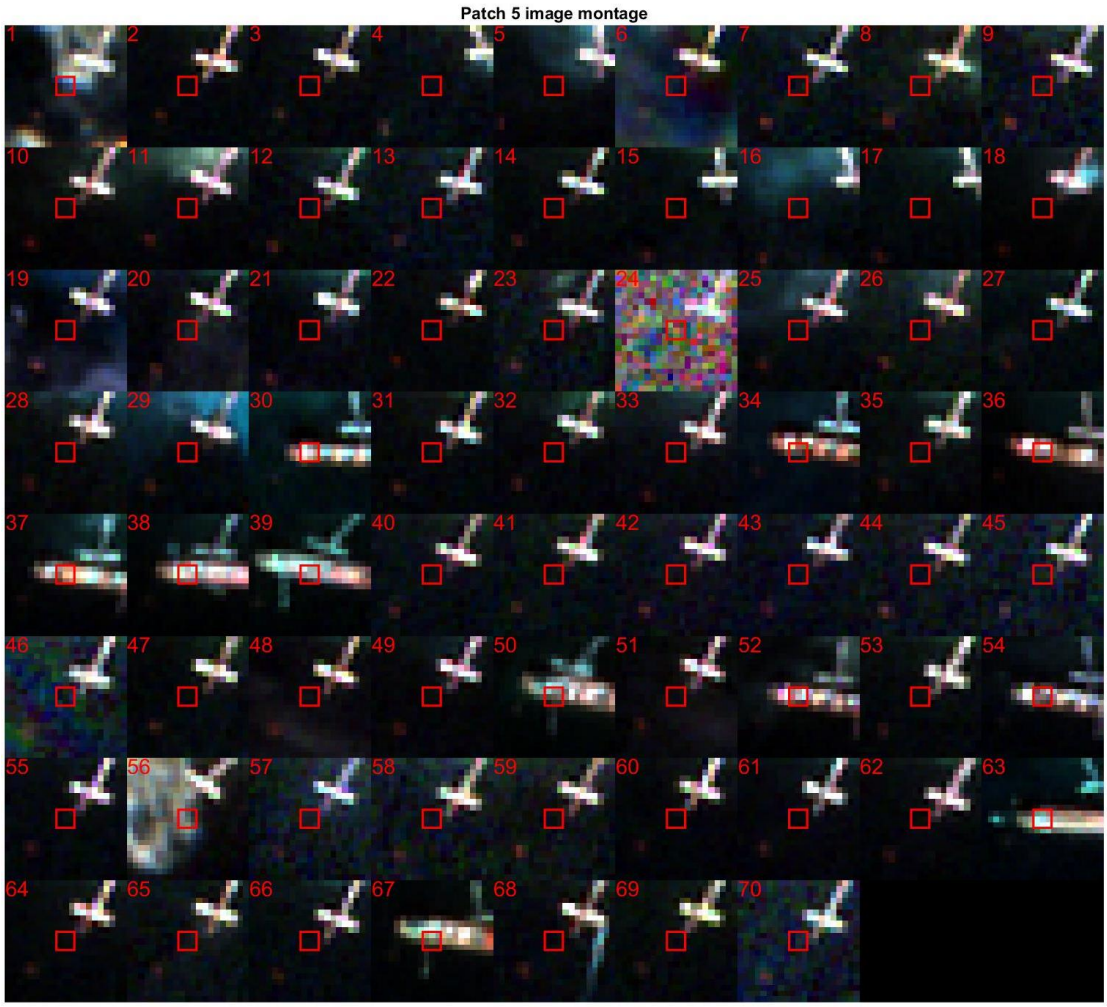

Figure 24: Patch 5 highlighted in red, background data = image 1-20, test data = image 21-70.

4.6. All patches

The overall performance of the RX-algorithm in this experiment is quite good, and it correctly classifies 91.9% of all pixels, and has 3.6% false negatives and 4.5% false positives.

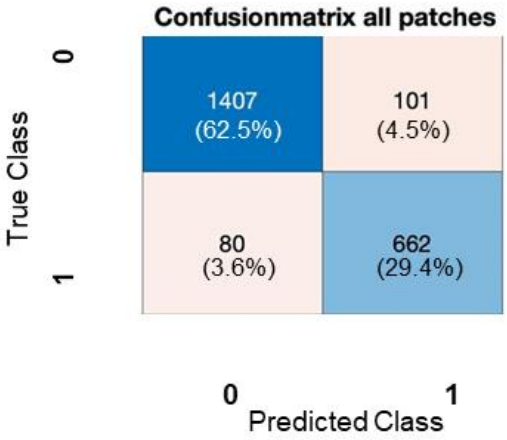

Figure 25: Confusion matrix for all patches.

When considering the distribution of false positives and false negatives between patches in *figure 26*, it is clear that patch 1 and 4 has a negative impact on the overall performance with their false negatives, and the high number of false positives in patch 1.

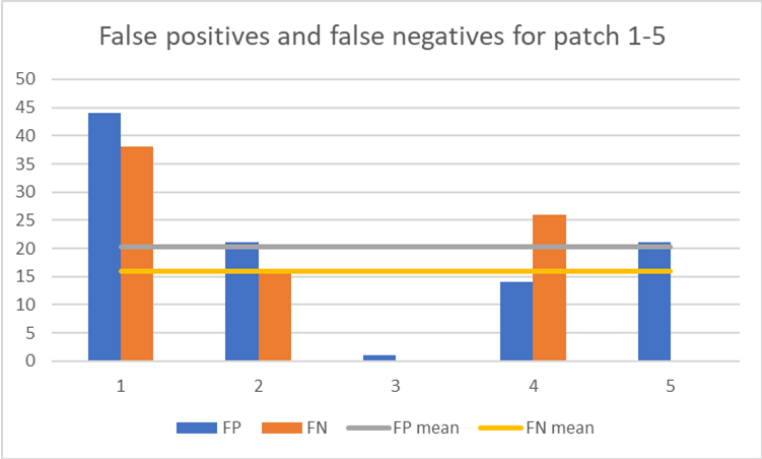

Figure 26: Number of false positives and negatives by patch with means drawn as lines.

When looking at F1, recall and precision in *table 1*, the performance is good. With a F1 score of 0.880 for the whole experiment the performance of the temporal RX-algorithm at pixel level is good. The recall is also quite acceptable across all patches with 0.675 on patch 4 and 0.764 on patch 1 as the lowest. The performance differs a lot between patches. The lowest precision is found on patch 1, with 0.737, and the rest are from 0.794 to 0.949. The performance on patch 1 and 4 is generally poorer than the rest on recall, precision and F1.

Patch	F1 score	Recall	Precision
1	0.750	0.764	0.737
2	0.955	0.961	0.949
3	0.947	1.000	0.900
4	0.730	0.675	0.794
5	0.891	1.000	0.804
Total	0.880	0.892	0.868

Table 1: Table with F1 scores, recall and precision for patch 1-5 and total.

Page intentionally left blank

5. Discussion

5.1. Mixed pixels and co-registration

The spatial distribution of misclassified pixels often coincides with the outlines of the changed areas. In patch 1 this is along the border between forest and construction site. In patch 2 the misclassifications are placed in the upper part of the 3x3 patch, which is the side that is closest to the natural vegetation. In patch 3 there are no predominant anomalies and no clear distribution. In patch 4 the distribution of misclassifications follows the shape of the bare soil. In patch 5 the misclassifications are most present along the edge between hull and water.

The spatial distribution of these misclassifications indicates that the temporal RX-algorithm performs poorer on abrupt changes between landcover. Mixed pixels are a reasonable explanation for this phenomenon. If the boat only covers 50% of the 10x10 meter pixel and the rest is water, the reflected value will not be only boat. The exact distribution of reflectance values from all the objects inside a pixel is hard to determine with a threshold value. It is possible that the temporal RX-algorithm classifies these mixed pixels better than the human eye, and that a human is more likely to visually interpret mixed pixels wrong.

Another problem is smaller objects within a pixel. If there is a car parked in a 10x10 meter pixel, it could potentially affect the measurements while being undetectable in the RGB image. It is likely that temporal RX-algorithm's performance is affected negatively by mixed pixels in this experiment.

There are indications of co-registration errors, but they are difficult to measure accurately due to the experiment design. One can also assume that the size of the time series incorporates the normal variation of the co-registration errors into the statistical backgrounds. As long as the co-registration error of the pixel under test is not significantly larger than the errors in the statistical model, the errors should not affect the performance significantly since the model includes the normal variation of the dataset. With the detection rate that the temporal RX-algorithm delivers on Sentinel-2 data the co-registration errors seem to have little effect on performance. It is possible that co-registration errors could contribute further to the mixed pixels problem at the edge between changed pixels and unchanged pixels.

The temporal RX-algorithm struggles most with performance on abrupt changes between two distinct types of landcover. It is likely that these edge problems are more problematic than co-registration errors and mixed pixels themselves, and that the previous mentioned errors further reduce performance along such edges.

The reduced performance along the edges of changes can, however, be used to infer that you should not expect the temporal RX-algorithm to perform well to detect anomalies before the size of the anomaly exceeds the spatial resolution of the images.

5.2. Scattered irradiance

The patches with the highest number of false negatives are patch 1 and 4. When inspecting these two images they both seem to contain more shadows than the rest. This indicates that the vegetation that surrounds the patches are higher than in the comparable patch 2 and 5. Irradiation caused by light bouncing from the vegetation could explain the errors. This phenomenon has been modelled and measured on a single tree and shows that the irradiance can affect NDVI scores (Kukenbrink, et al., 2019). The scattering effects differs through the spectrum and decreases with increased distance from the tree. The model used by Kukenbrink et al. (2019) displays an effect several meters from just a single tree.

In patch 4, irradiance from the surrounding trees could potentially mask the bare soil visible in the RGB band with IR vegetation values from neighbouring pixels. This could possibly lead to false negatives, since the statistical models contains pixels containing vegetation, and a high number of IR-bands are used in the experiment.

5.3. Difference between patches

The patches were selected to test different aspects of the temporal RX-algorithm. Patch 1 and 2, which both contain a windmill under construction, have very different results. The deliberate centre placement of patch 2 on the known change seems to increase the performance significantly when compared to the deliberate edge placement of patch 1.

Patches 1 and 4 also share some of the characteristics. They both have an edge placement, and they have more shadows than patch 2. The fact that patch 1 contains a manmade object, while patch 4 only uncovers bare soil does not seem to change the performance. Patch 3 that contains no known anomalous changes, and patch 5 with appearing and disappearing anomalous changes, are the two with no false negatives.

5.4. General performance

At its best, the temporal RX-algorithm performs very well. This is evident in patch 2. On the very similar patch 1, the performance is significantly poorer. This is expected since this patch has a higher potential of mixed pixels, co-registration errors, and scattered irradiance. However, the overall performance is good. This indicates that the temporal RX-algorithm could be further refined to be used in surveillance systems given that the data is sufficiently pre-processed. The performance indicates that there is a need of a human to study the areas classified with anomalies afterwards. Still, it would reduce the human labour needed to study images when detecting anomalous changes.

This study has not compared temporal-RX with different change detection methods. It is hard to determine which methods that are most precise. The temporal-RX approach has most in common with pixel-based methods and Median Filtering-Based Background Formation. It operates on pixel level but uses a statistical background to determine anomalies rather than deviations from the median. The advantage of the temporal-RX is that different image bands can be added or subtracted from the model, and the training data can be adjusted. This means that it can be somewhat tailored to be either very specific and sensitive, or more generic and less sensitive. The greatest potential with temporal-RX could be the use of Gaussian mixture models to model several normal seasons. This can be used to tailor better models for areas with large seasonal variations or incorporate normal elements such as red boats in a harbour, but not blue.

5.5. Limitations of the study

The process of ground truthing depends on a visual interpretation of pixels. Since this is a subjective process, it could introduce errors. To determine the border between water and boat, or the border between forest and road is difficult. Especially when the images contain different amounts of shadows and light.

A better method would have been to introduce known changes, such as a 10x10 meter tarpon, into the study area. This gives full control over the change and the position of the object. This method would also increase the possibility to measure co-registration errors and control mixed pixels by aligning the tarpon inside a 10x10

meter pixel if it is possible. Since this requires long-term planning and physical access to the area, it has not been possible to do in this research.

The resolution of the images is 10x10 meters. It is possible that sub-pixel anomalies are detected by the temporal RX-algorithm with data from other bands that has not been used for the visual classification. Without access to pictures from the area, or controlled observations on the ground, it is hard to control the existence of sub-pixel objects.

The study has been conducted on Sentinel-2 1C data that contains top-of-atmosphere reflectance, not 2A data that is processed to contain surface reflectance. This could possibly reduce the data quality of the ground objects. However, this study indicates that the performance on top-of-atmosphere data is quite good. Since the statistical model from the training data is drawn from a several images taken under different atmospheric reflectance, it is possible that the errors are generalized into the model. However, 2A data would be preferred above 1C data for detection of objects at ground level.

The pre-processing is done manually and many of the available images have been discarded. The result is that both the background models and test pixels are quite clean. This could make the detector more sensitive to natural errors such as the hue phenomena visible in patch 5 image 24 and increase the false positive rate. Another problem is that the performance of the algorithm in the experiment is heavily dependent on pre-processing. The data must either be quality controlled manually, or with a robust automated pre-processing suitable for the purpose.

The high number of discarded images has also reduced the size of the dataset. Since the construction of the windmill starts in image 23 of the 70 approved ones, the upper limit of images to include in the training data was 22. I found it reasonable to include a few images without known changes in the test data for the two patches with windmills, and the images used to model the background pixels were limited to 20. A longer time series, where assumed natural errors such as the one in image 24 are included, could potentially give better background models reduce the number of false positives, and would make the performance more robust.

5.6. Suggestions for further research

The temporal RX-algorithm seems to work well on quality-controlled images where the anomalous changes extend at least across the pixel resolution. To increase the performance further research is suggested to focus on:

1) Pre-processing of Sentinel-2 images to ensure that images are good enough to be used for this type of automated classification.
2) Methods to mitigate classification errors on the border between changed and unchanged pixels. This could include both sub-pixel detection, morphological methods such as opening or by experimenting with the temporal RX-algorithm, where parts of the spatial neighbourhood are included along with the temporal dimension.
3) Testing if false negatives can be reduced by adjusting band composition when using the temporal RX-algorithm on areas surrounded by high trees.
4) Since the temporal RX-algorithm works with one statistical distribution, it would be interesting to see how Gaussian mixture models performs across different seasonal changes. It should be possible to have separate models for spring, summer, fall and winter.

Page intentionally left blank

6. Conclusions

6.1. Objective 1

6.1.1. Q1.1

The temporal RX-algorithm implemented on Sentinel-2 images in this assignment can detect anomalous changes at pixel level in different environmental conditions. It can be applied on images containing water and vegetation, and can detect vegetation to soil, vegetation to manmade construction, and water to boat changes.

6.1.2. Q1.2

The changes that the temporal RX-algorithm detects are quite consistent with the time stamps of the images. The changes detected coincides well with the visually detectable changes in the images. This is most clear in patch 5, where the changes are temporary (moving boats) and not changing from one state to another.

6.2. Objective 2

6.2.1. Q2.1

The temporal RX-algorithm implemented in this experiment detects anomalous changes at 10x10 meter resolution with a total of 3.6% false negatives and 4.5% false positives. The total number of analysed and classified pixels are 2250, with 80 false negatives and 101 false positives. The recall is 0.892, precision is 0.868 and F1 is 0.880. On each patch the metrics varies with a significantly higher number of errors in patch 1 and 4.

6.2.2. Q2.2

The spatial distribution of the errors seems to follow the borders of the changes. Meaning that the number of errors increases in the outer edges of the changed areas, and that the temporal RX-algorithm performs best to detect changes with a spatial extent of at least one pixel.

6.3. Conclusion summary

The experiment shows that the temporal RX-algorithm performs quite well for detecting changes in Sentinel-2 images using all bands except band 9 and 10. It works with images containing more challenging terrain than desert, and on temporary changes like boats, and on areas which changes from one state to another. The temporal RX-algorithm performs best when the changes are larger than the spatial resolution of the images. Borders between changed and unchanged areas are most challenging. This implies that a mixture of co-registration errors, mixed pixels and scattered irradiance may affect the performance.

When considering the time a human would need to classify the same amount of pixels, the approach shows promising results as a cost-effective aid to imagery analysts in their work.

6.4. Possible applications

The temporal RX-algorithm shows a potential for application within automated or semi-automated surveillance systems. It could be to identify emerging permanent constructions, or temporal placement of objects such as docking of boats. The most crucial limitations are spatial and temporal resolution. This thesis shows suboptimal performance when pixels are not fully saturated with the change. Robust detection of

smaller objects than the spatial resolution of the images cannot be expected when used as in this thesis. The high number of discarded images reduces the temporal resolution and makes the temporal RX-algorithm less suitable for detection of temporal object such as boats – since many images with potential boats are discarded. It can detect them, but the time series are incomplete, and reliability of the system is reduced.

Another application is to aid imagery analysts to find areas of interest. With increasing amounts of image data, time spent by humans inspecting images is increasingly scarce. A workflow that uses an implementation of the temporal RX-algorithm could help analysts find the relevant focus areas, and discard areas without flagged anomalies. For this application, an adjustment of the threshold to achieve a higher false positive rate to suppress false negatives could be preferable since humans could remove false positives, but not negatives.

To implement the temporal RX-algorithm into an automated system, several other processing steps must be added. It seems like automated pre-processing and quality control would be the most beneficial. The temporal RX-algorithm must also be implemented differently to produce anomaly rasters, like the detection maps used by (Ziemann, Simonoko, & Flynn, 2020).

References

Acito, N., Diani , M., Corsini, G., & Resta, S. (2017, July). "Introductory view of anomalous change detection in hyperspectral images within a theoretical gaussian framework," . *IEEE Aerospace and Electronic Systems Magazine, vol. 32, no. 7*, pp. pp. 2-27.

Brereton, R. (2014). The chi squared and multinormal distributions. *J. Chemometrics, 29*, 9-12.

Decuyper, M., Chávez, R., Lohbeck, M., Lastra, J., Tsendbazar, N., Hackländer, J., . . . Vågen, T.-G. (2022). *"Continuous monitoring of forest change dynamics with satellite time series."* . Remote Sensing of Environment, 269.

Doshi, N., Koringa, P., & Ghosh, R. (2020). "Geometric and Radiometric Assessment of Sentinel-2A and Sentinel-2B sensors,". *2020 7th International Conference on Signal Processing and Integrated Networks (SPIN),*, (pp. pp. 975-980).

Eismann, M. (2012). *"Hyperspectral remote sensing"*. SPIE press.

Ekiz, M., & Ekiz, O. (2017). Outlier detection with Mahalanobis square distance: incorporating small sample correction factor. *Journal of Applied Statistics ;44(13):*, 2444-2457.

Elkholy, M., Mostafa, M., ElSayad, D., Ebeid, H., & Tolba, M. (2023). Convolutional Autoencoder for Remote Sensing Change Detection. *Springer Proceedings in Earth and Environmental Sciences*.

El-Rewainy, A., & Farouk, E. (2011). Improvement of RX Algorithm Performance in Anomaly Detection Applied on Hyperspectral Imaging. *AEROSPACE SCIENCES & AVIATION TECHNOLOGY, ASAT - 14.*

Esa. (2024, Februar 16). *Sentinel Online*. Retrieved from Processing Levels: https://sentinel.esa.int/web/sentinel/user-guides/sentinel-2-msi/processing-levels

European Space Agency. (2015, March). *Sentinel-2 Data Access and Products Fact Sheet.* Retrieved from https://sentinel.esa.int/web/sentinel/missions/sentinel-2/instrument-payload/resolution-and-swath

European Space Agency. (2015, July 24). Sentinel-2 User Handbook. Retrieved from https://sentinel.esa.int/documents/247904/685211/Sentinel-2_User_Handbook

Geethika, G., Sreeja, V., Tharuni, T., & Radhesyam, V. (2024). Vegetation Change Detection of Multispectral Satellite Images Using Remote Sensing. *Singapore: Springer Nature Singapore (Lecture Notes in Electrical Engineering. 1087)*, 337-349.

Gevers, T., & Smeulders, A. (1997). Color based object recognition. *Image Analysis and Processing*, pp. 319-326.

Hupel, T., & Stütz, P. (2022). "Adopting Hyperspectral Anomaly Detection for Near Real-Time Camouflage Detection in Multispectral Imagery". *Remote Sensing, 14(15),*, p. p. 3755.

İlsever, M. (2012). *Two-Dimensional Change Detection Methods. Remote Sensing Applications. Edited by Cem Ünsalan. 1st ed.* Springer London. : SpringerBriefs in Computer Science. .

Kukenbrink, D., Hueni, A., Schneider, F., Damm, A., Gastellu-Etchegorry, J., Schaepman, M., & Morsdorf, F. (2019). Mapping the irradiance field of a single tree: quantifying vegetation-induced adjacency effects. *IEEE Transactions on Geoscience and Remote Sensing, 57(7)*, 4994–5011.

Lu, D., Moran, E., Mausel, P., & Brondízio, E. (2004). Change detection techniques. *International Journal of Remote Sensing, vol. 25, no. 12,*, pp. 2365-2401.

Manolakis, D. G. (2002). *"Overview of algorithms for hyperspectral target detection: theory and practice".* Proc. SPIE 4725, Algorithms and Technologies for Multispectral, Hyperspectral, and Ultraspectral Imagery VIII.

Matteoli, S., Diani, M., & Corsini, G. (2010). "A tutorial overview of anomaly detection in hyperspectral images". *IEEE A&E Systems Magazine, vol. 25*, pp. pp. 5-27.

Meola, J., & Eismann, M. (2008). "Image misregistration effects on hyperspectral change detection,". *Proc. SPIE 6966, Algorithms and Technologies for Multispectral, Hyperspectral, and Ultraspectral Imagery XIV, 69660Y.* SPIE.

NVE. (2022, 11 11). *NVE temakart*. Retrieved from NVE vindkraft: https://temakart.nve.no/tema/vindkraftverk

Reed, I. S., & Yu, X. (1990, Oct.). "Adaptive multiple-band CFAR detection of an optical pattern with unknown spectral distribution". *IEEE Trans. on Acoustics Speech and Sig. Proc., vol. 38, no. 10*, pp. 1760-1770.

Simonoko, H., Ziemann, A., & Flynn, E. (2020). *"Investigating temporal distributions for spectral anomaly detection through time".* Proc. SPIE 11392, Algorithms, Technologies, and Applications for Multispectral and Hyperspectral Imagery XXVI, 113920X .

Singh, A. (1989). Review article: digital change detection techniques using remotely-sensed data. *Int. J. Remote Sens. 10(6)*, pp. 989–1003.

Tharwat, A. (2020). “Classification assessment methods”,. *New England Journal of Entrepreneurship. Vol. 17 No. 1*, pp. pp. 168-192.

Theiler, J., & Wohlberg, B. (2012). Local Coregistration Adjustment for Anomalous Change Detection. *IEEE Transactions on Geoscience and Remote Sensing, Geoscience and Remote Sensing, IEEE Transactions on, IEEE Trans. Geosci. Remote Sensing, 50(8)*, pp. 3107–3116.

Tomowski, D., Klonus, S., Ehlers, M., Michel, U., & Reinartz, P. (2010). Change Visualization Through A Texture-Based Analysis Approach. *Proceedings of ISPRS Technical Commission VII Symposium-100 Years ISPRS Advancing Remote Sensing Science Sensing, vol. 38*, (pp. 263–268). Vienna.

Verhoeven, G. (2018). Multispectral and Hyperspectral Imaging. In S. (. López Varela, *The Encyclopedia of Archaeological Sciences.* John Wiley & Sons.

Wu, C., Zhang, L., & Du, B. (2015). "Hyperspectral anomaly change detection with slow feature analysis". *Neurocomputing, Volume 151, Part 1,*, pp. Pages 175-187.

Zhan, Y., Fu, K., Yan, M., Sun, X., Wang, H., & Qiu, X. (2017). Change Detection Based on Deep Siamese Convolutional Network for Optical Aerial Images. *IEEE Geoscience and Remote Sensing Letters, Geoscience and Remote Sensing Letters, IEEE, IEEE Geosci. Remote Sensing Lett, vol. 14, no. 10*, 1845–1849.

Zhao, G., Shan, L., & Wang, W. (2023). End-to-end Remote Sensing Change Detection of Unregistered Bi-temporal Images for Natural Disasters. *32nd International Conference on Artificial Neural Networks* (pp. 259-270). Heraklion: Springer.

Ziemann, A., Simonoko, H., & Flynn, E. (2020). *"Temporal Anomaly Detection in Multispectral Imagery,".* IGARSS 2020 - 2020 IEEE International Geoscience and Remote Sensing Symposium,.

Annex A – List with image dates

Image_number	Image taken (YYYYMMDD)
1	'20150725'
2	'20150818'
3	'20150824'
4	'20150903'
5	'20160527'
6	'20160606'
7	'20161014'
8	'20161021'
9	'20161024'
10	'20170628'
11	'20170719'
12	'20170825'
13	'20170926'
14	'20180517'
15	'20180525'
16	'20180530'
17	'20180606'
18	'20180608'
19	'20180629'
20	'20180701'
21	'20180704'
22	'20180726'
23	'20181029'
24	'20181120'
25	'20190404'
26	'20190405'
27	'20190407'
28	'20190409'
29	'20190410'
30	'20190412'
31	'20190414'
32	'20190415'
33	'20190424'
34	'20190611'
35	'20190713'

Image_number	Image taken (YYYYMMDD)
36	'20190716'
37	'20190726'
38	'20190728'
39	'20190921'
40	'20190924'
41	'20190926'
42	'20191004'
43	'20191006'
44	'20191014'
45	'20191103'
46	'20191105'
47	'20200529'
48	'20200531'
49	'20200615'
50	'20200723'
51	'20200725'
52	'20200809'
53	'20200816'
54	'20200826'
55	'20200831'
56	'20200926'
57	'20201003'
58	'20201015'
59	'20201016'
60	'20210528'
61	'20210529'
62	'20210622'
63	'20210630'
64	'20210702'
65	'20210723'
66	'20210725'
67	'20210730'
68	'20210822'
69	'20210826'
70	'20211104'

Series from Lund University

Department of Physical Geography and Ecosystem Science

Master Thesis in Geographical Information Science

1. *Anthony Lawther*: The application of GIS-based binary logistic regression for slope failure susceptibility mapping in the Western Grampian Mountains, Scotland (2008).
2. *Rickard Hansen*: Daily mobility in Grenoble Metropolitan Region, France. Applied GIS methods in time geographical research (2008).
3. *Emil Bayramov*: Environmental monitoring of bio-restoration activities using GIS and Remote Sensing (2009).
4. *Rafael Villarreal Pacheco*: Applications of Geographic Information Systems as an analytical and visualization tool for mass real estate valuation: a case study of Fontibon District, Bogota, Columbia (2009).
5. *Siri Oestreich Waage*: a case study of route solving for oversized transport: The use of GIS functionalities in transport of transformers, as part of maintaining a reliable power infrastructure (2010).
6. *Edgar Pimiento*: Shallow landslide susceptibility – Modelling and validation (2010).
7. *Martina Schäfer*: Near real-time mapping of floodwater mosquito breeding sites using aerial photographs (2010).
8. *August Pieter van Waarden-Nagel*: Land use evaluation to assess the outcome of the programme of rehabilitation measures for the river Rhine in the Netherlands (2010).
9. *Samira Muhammad*: Development and implementation of air quality data mart for Ontario, Canada: A case study of air quality in Ontario using OLAP tool (2010).
10. *Fredros Oketch Okumu*: Using remotely sensed data to explore spatial and temporal relationships between photosynthetic productivity of vegetation and malaria transmission intensities in selected parts of Africa (2011).
11. *Svajunas Plunge*: Advanced decision support methods for solving diffuse water pollution problems (2011).
12. *Jonathan Higgins*: Monitoring urban growth in greater Lagos: A case study using GIS to monitor the urban growth of Lagos 1990 - 2008 and produce future growth prospects for the city (2011).
13. *Mårten Karlberg*: Mobile Map Client API: Design and Implementation for Android (2011).
14. *Jeanette McBride*: Mapping Chicago area urban tree canopy using color infrared imagery (2011).
15. *Andrew Farina*: Exploring the relationship between land surface temperature and vegetation abundance for urban heat island mitigation in Seville, Spain (2011).
16. *David Kanyari*: Nairobi City Journey Planner: An online and a Mobile Application (2011).
17. *Laura V. Drews*: Multi-criteria GIS analysis for siting of small wind power plants - A case study from Berlin (2012).
18. *Qaisar Nadeem*: Best living neighborhood in the city - A GIS based multi criteria evaluation of ArRiyadh City (2012).

19. *Ahmed Mohamed El Saeid Mustafa*: Development of a photo voltaic building rooftop integration analysis tool for GIS for Dokki District, Cairo, Egypt (2012).
20. *Daniel Patrick Taylor*: Eastern Oyster Aquaculture: Estuarine Remediation via Site Suitability and Spatially Explicit Carrying Capacity Modeling in Virginia's Chesapeake Bay (2013).
21. *Angeleta Oveta Wilson*: A Participatory GIS approach to unearthing Manchester's Cultural Heritage 'gold mine' (2013).
22. *Ola Svensson*: Visibility and Tholos Tombs in the Messenian Landscape: A Comparative Case Study of the Pylian Hinterlands and the Soulima Valley (2013).
23. *Monika Ogden*: Land use impact on water quality in two river systems in South Africa (2013).
24. *Stefan Rova*: A GIS based approach assessing phosphorus load impact on Lake Flaten in Salem, Sweden (2013).
25. *Yann Buhot*: Analysis of the history of landscape changes over a period of 200 years. How can we predict past landscape pattern scenario and the impact on habitat diversity? (2013).
26. *Christina Fotiou*: Evaluating habitat suitability and spectral heterogeneity models to predict weed species presence (2014).
27. *Inese Linuza*: Accuracy Assessment in Glacier Change Analysis (2014).
28. *Agnieszka Griffin*: Domestic energy consumption and social living standards: a GIS analysis within the Greater London Authority area (2014).
29. *Brynja Guðmundsdóttir*: Detection of potential arable land with remote sensing and GIS - A Case Study for Kjósarhreppur (2014).
30. *Oleksandr Nekrasov*: Processing of MODIS Vegetation Indices for analysis of agricultural droughts in the southern Ukraine between the years 2000-2012 (2014).
31. *Sarah Tressel*: Recommendations for a polar Earth science portal in the context of Arctic Spatial Data Infrastructure (2014).
32. *Caroline Gevaert*: Combining Hyperspectral UAV and Multispectral Formosat-2 Imagery for Precision Agriculture Applications (2014).
33. *Salem Jamal-Uddeen*: Using GeoTools to implement the multi-criteria evaluation analysis - weighted linear combination model (2014).
34. *Samanah Seyedi-Shandiz*: Schematic representation of geographical railway network at the Swedish Transport Administration (2014).
35. *Kazi Masel Ullah*: Urban Land-use planning using Geographical Information System and analytical hierarchy process: case study Dhaka City (2014).
36. *Alexia Chang-Wailing Spitteler*: Development of a web application based on MCDA and GIS for the decision support of river and floodplain rehabilitation projects (2014).
37. *Alessandro De Martino*: Geographic accessibility analysis and evaluation of potential changes to the public transportation system in the City of Milan (2014).
38. *Alireza Mollasalehi*: GIS Based Modelling for Fuel Reduction Using Controlled Burn in Australia. Case Study: Logan City, QLD (2015).
39. *Negin A. Sanati*: Chronic Kidney Disease Mortality in Costa Rica; Geographical Distribution, Spatial Analysis and Non-traditional Risk Factors (2015).

40. *Karen McIntyre*: Benthic mapping of the Bluefields Bay fish sanctuary, Jamaica (2015).
41. *Kees van Duijvendijk*: Feasibility of a low-cost weather sensor network for agricultural purposes: A preliminary assessment (2015).
42. *Sebastian Andersson Hylander*: Evaluation of cultural ecosystem services using GIS (2015).
43. *Deborah Bowyer*: Measuring Urban Growth, Urban Form and Accessibility as Indicators of Urban Sprawl in Hamilton, New Zealand (2015).
44. *Stefan Arvidsson*: Relationship between tree species composition and phenology extracted from satellite data in Swedish forests (2015).
45. *Damián Giménez Cruz*: GIS-based optimal localisation of beekeeping in rural Kenya (2016).
46. *Alejandra Narváez Vallejo*: Can the introduction of the topographic indices in LPJ-GUESS improve the spatial representation of environmental variables? (2016).
47. *Anna Lundgren*: Development of a method for mapping the highest coastline in Sweden using breaklines extracted from high resolution digital elevation models (2016).
48. *Oluwatomi Esther Adejoro*: Does location also matter? A spatial analysis of social achievements of young South Australians (2016).
49. *Hristo Dobrev Tomov*: Automated temporal NDVI analysis over the Middle East for the period 1982 - 2010 (2016).
50. *Vincent Muller*: Impact of Security Context on Mobile Clinic Activities A GIS Multi Criteria Evaluation based on an MSF Humanitarian Mission in Cameroon (2016).
51. *Gezahagn Negash Seboka*: Spatial Assessment of NDVI as an Indicator of Desertification in Ethiopia using Remote Sensing and GIS (2016).
52. *Holly Buhler*: Evaluation of Interfacility Medical Transport Journey Times in Southeastern British Columbia. (2016).
53. *Lars Ole Grottenberg*: Assessing the ability to share spatial data between emergency management organisations in the High North (2016).
54. *Sean Grant*: The Right Tree in the Right Place: Using GIS to Maximize the Net Benefits from Urban Forests (2016).
55. *Irshad Jamal*: Multi-Criteria GIS Analysis for School Site Selection in Gorno- Badakhshan Autonomous Oblast, Tajikistan (2016).
56. *Fulgencio Sanmartín*: Wisdom-volkano: A novel tool based on open GIS and time-series visualization to analyse and share volcanic data (2016).
57. *Nezha Acil*: Remote sensing-based monitoring of snow cover dynamics and its influence on vegetation growth in the Middle Atlas Mountains (2016).
58. *Julia Hjalmarsson*: A Weighty Issue: Estimation of Fire Size with Geographically Weighted Logistic Regression (2016).
59. *Mathewos Tamiru Amato*: Using multi-criteria evaluation and GIS for chronic food and nutrition insecurity indicators analysis in Ethiopia (2016).
60. *Karim Alaa El Din Mohamed Soliman El Attar*: Bicycling Suitability in Downtown, Cairo, Egypt (2016).
61. *Gilbert Akol Echelai*: Asset Management: Integrating GIS as a Decision Support Tool in Meter Management in National Water and Sewerage Corporation (2016).
62. *Terje Slinning*: Analytic comparison of multibeam echo soundings (2016).

63. *Gréta Hlín Sveinsdóttir*: GIS-based MCDA for decision support: A framework for wind farm siting in Iceland (2017).
64. *Jonas Sjögren*: Consequences of a flood in Kristianstad, Sweden: A GIS-based analysis of impacts on important societal functions (2017).
65. *Nadine Raska*: 3D geologic subsurface modelling within the Mackenzie Plain, Northwest Territories, Canada (2017).
66. *Panagiotis Symeonidis*: Study of spatial and temporal variation of atmospheric optical parameters and their relation with PM 2.5 concentration over Europe using GIS technologies (2017).
67. *Michaela Bobeck*: A GIS-based Multi-Criteria Decision Analysis of Wind Farm Site Suitability in New South Wales, Australia, from a Sustainable Development Perspective (2017).
68. *Raghdaa Eissa*: Developing a GIS Model for the Assessment of Outdoor Recreational Facilities in New Cities Case Study: Tenth of Ramadan City, Egypt (2017).
69. *Zahra Khais Shahid*: Biofuel plantations and isoprene emissions in Svea and Götaland (2017).
70. *Mirza Amir Liaquat Baig*: Using geographical information systems in epidemiology: Mapping and analyzing occurrence of diarrhea in urban - residential area of Islamabad, Pakistan (2017).
71. *Joakim Jörwall*: Quantitative model of Present and Future well-being in the EU-28: A spatial Multi-Criteria Evaluation of socioeconomic and climatic comfort factors (2017).
72. *Elin Haettner*: Energy Poverty in the Dublin Region: Modelling Geographies of Risk (2017).
73. *Harry Eriksson*: Geochemistry of stream plants and its statistical relations to soil- and bedrock geology, slope directions and till geochemistry. A GIS-analysis of small catchments in northern Sweden (2017).
74. *Daniel Gardevärn*: PPGIS and Public meetings – An evaluation of public participation methods for urban planning (2017).
75. *Kim Friberg*: Sensitivity Analysis and Calibration of Multi Energy Balance Land Surface Model Parameters (2017).
76. *Viktor Svanerud*: Taking the bus to the park? A study of accessibility to green areas in Gothenburg through different modes of transport (2017).
77. *Lisa-Gaye Greene*: Deadly Designs: The Impact of Road Design on Road Crash Patterns along Jamaica's North Coast Highway (2017).
78. *Katarina Jemec Parker*: Spatial and temporal analysis of fecal indicator bacteria concentrations in beach water in San Diego, California (2017).
79. *Angela Kabiru*: An Exploratory Study of Middle Stone Age and Later Stone Age Site Locations in Kenya's Central Rift Valley Using Landscape Analysis: A GIS Approach (2017).
80. *Kristean Björkmann*: Subjective Well-Being and Environment: A GIS-Based Analysis (2018).
81. *Williams Erhunmonmen Ojo*: Measuring spatial accessibility to healthcare for people living with HIV-AIDS in southern Nigeria (2018).
82. *Daniel Assefa*: Developing Data Extraction and Dynamic Data Visualization (Styling) Modules for Web GIS Risk Assessment System (WGRAS). (2018).
83. *Adela Nistora*: Inundation scenarios in a changing climate: assessing potential impacts of sea-level rise on the coast of South-East England (2018).

84. *Marc Seliger*: Thirsty landscapes - Investigating growing irrigation water consumption and potential conservation measures within Utah's largest master-planned community: Daybreak (2018).
85. *Luka Jovičić*: Spatial Data Harmonisation in Regional Context in Accordance with INSPIRE Implementing Rules (2018).
86. *Christina Kourdounouli*: Analysis of Urban Ecosystem Condition Indicators for the Large Urban Zones and City Cores in EU (2018).
87. *Jeremy Azzopardi*: Effect of distance measures and feature representations on distance-based accessibility measures (2018).
88. *Patrick Kabatha*: An open source web GIS tool for analysis and visualization of elephant GPS telemetry data, alongside environmental and anthropogenic variables (2018).
89. *Richard Alphonce Giliba*: Effects of Climate Change on Potential Geographical Distribution of Prunus africana (African cherry) in the Eastern Arc Mountain Forests of Tanzania (2018).
90. *Eiður Kristinn Eiðsson*: Transformation and linking of authoritative multi-scale geodata for the Semantic Web: A case study of Swedish national building data sets (2018).
91. *Niamh Harty*: HOP!: a PGIS and citizen science approach to monitoring the condition of upland paths (2018).
92. *José Estuardo Jara Alvear*: Solar photovoltaic potential to complement hydropower in Ecuador: A GIS-based framework of analysis (2018).
93. *Brendan O'Neill*: Multicriteria Site Suitability for Algal Biofuel Production Facilities (2018).
94. *Roman Spataru*: Spatial-temporal GIS analysis in public health – a case study of polio disease (2018).
95. *Alicja Miodońska*: Assessing evolution of ice caps in Suðurland, Iceland, in years 1986 - 2014, using multispectral satellite imagery (2019).
96. *Dennis Lindell Schettini*: A Spatial Analysis of Homicide Crime's Distribution and Association with Deprivation in Stockholm Between 2010-2017 (2019).
97. *Damiano Vesentini*: The Po Delta Biosphere Reserve: Management challenges and priorities deriving from anthropogenic pressure and sea level rise (2019).
98. *Emilie Arnesten*: Impacts of future sea level rise and high water on roads, railways and environmental objects: a GIS analysis of the potential effects of increasing sea levels and highest projected high water in Scania, Sweden (2019).
99. *Syed Muhammad Amir Raza*: Comparison of geospatial support in RDF stores: Evaluation for ICOS Carbon Portal metadata (2019).
100. *Hemin Tofiq*: Investigating the accuracy of Digital Elevation Models from UAV images in areas with low contrast: A sandy beach as a case study (2019).
101. *Evangelos Vafeiadis*: Exploring the distribution of accessibility by public transport using spatial analysis. A case study for retail concentrations and public hospitals in Athens (2019).
102. *Milan Sekulic*: Multi-Criteria GIS modelling for optimal alignment of roadway by-passes in the Tlokweng Planning Area, Botswana (2019).
103. *Ingrid Piirisaar*: A multi-criteria GIS analysis for siting of utility-scale photovoltaic solar plants in county Kilkenny, Ireland (2019).

104. *Nigel Fox*: Plant phenology and climate change: possible effect on the onset of various wild plant species' first flowering day in the UK (2019).
105. *Gunnar Hesch*: Linking conflict events and cropland development in Afghanistan, 2001 to 2011, using MODIS land cover data and Uppsala Conflict Data Programme (2019).
106. *Elijah Njoku*: Analysis of spatial-temporal pattern of Land Surface Temperature (LST) due to NDVI and elevation in Ilorin, Nigeria (2019).
107. *Katalin Bunyevácz*: Development of a GIS methodology to evaluate informal urban green areas for inclusion in a community governance program (2019).
108. *Paul dos Santos*: Automating synthetic trip data generation for an agent-based simulation of urban mobility (2019).
109. *Robert O' Dwyer*: Land cover changes in Southern Sweden from the mid-Holocene to present day: Insights for ecosystem service assessments (2019).
110. *Daniel Klingmyr*: Global scale patterns and trends in tropospheric NO2 concentrations (2019).
111. *Marwa Farouk Elkabbany*: Sea Level Rise Vulnerability Assessment for Abu Dhabi, United Arab Emirates (2019).
112. *Jip Jan van Zoonen*: Aspects of Error Quantification and Evaluation in Digital Elevation Models for Glacier Surfaces (2020).
113. *Georgios Efthymiou*: The use of bicycles in a mid-sized city – benefits and obstacles identified using a questionnaire and GIS (2020).
114. *Haruna Olayiwola Jimoh*: Assessment of Urban Sprawl in MOWE/IBAFO Axis of Ogun State using GIS Capabilities (2020).
115. *Nikolaos Barmpas Zachariadis*: Development of an iOS, Augmented Reality for disaster management (2020).
116. *Ida Storm*: ICOS Atmospheric Stations: Spatial Characterization of CO2 Footprint Areas and Evaluating the Uncertainties of Modelled CO2 Concentrations (2020).
117. *Alon Zuta*: Evaluation of water stress mapping methods in vineyards using airborne thermal imaging (2020).
118. *Marcus Eriksson*: Evaluating structural landscape development in the municipality Upplands-Bro, using landscape metrics indices (2020).
119. *Ane Rahbek Vierø*: Connectivity for Cyclists? A Network Analysis of Copenhagen's Bike Lanes (2020).
120. *Cecilia Baggini*: Changes in habitat suitability for three declining Anatidae species in saltmarshes on the Mersey estuary, North-West England (2020).
121. *Bakrad Balabanian*: Transportation and Its Effect on Student Performance (2020).
122. *Ali Al Farid*: Knowledge and Data Driven Approaches for Hydrocarbon Microseepage Characterizations: An Application of Satellite Remote Sensing (2020).
123. *Bartlomiej Kolodziejczyk*: Distribution Modelling of Gene Drive-Modified Mosquitoes and Their Effects on Wild Populations (2020).
124. *Alexis Cazorla*: Decreasing organic nitrogen concentrations in European water bodies - links to organic carbon trends and land cover (2020).
125. *Kharid Mwakoba*: Remote sensing analysis of land cover/use conditions of community-based wildlife conservation areas in Tanzania (2021).
126. *Chinatsu Endo*: Remote Sensing Based Pre-Season Yellow Rust Early Warning in Oromia, Ethiopia (2021).

127. *Berit Mohr*: Using remote sensing and land abandonment as a proxy for long- term human out-migration. A Case Study: Al-Hassakeh Governorate, Syria (2021).
128. *Kanchana Nirmali Bandaranayake*: Considering future precipitation in delineation locations for water storage systems - Case study Sri Lanka (2021).
129. *Emma Bylund*: Dynamics of net primary production and food availability in the aftermath of the 2004 and 2007 desert locust outbreaks in Niger and Yemen (2021).
130. *Shawn Pace*: Urban infrastructure inundation risk from permanent sea-level rise scenarios in London (UK), Bangkok (Thailand) and Mumbai (India): A comparative analysis (2021).
131. *Oskar Evert Johansson*: The hydrodynamic impacts of Estuarine Oyster reefs, and the application of drone technology to this study (2021).
132. *Pritam Kumarsingh*: A Case Study to develop and test GIS/SDSS methods to assess the production capacity of a Cocoa Site in Trinidad and Tobago (2021).
133. *Muhammad Imran Khan*: Property Tax Mapping and Assessment using GIS (2021).
134. *Domna Kanari*: Mining geosocial data from Flickr to explore tourism patterns: The case study of Athens (2021).
135. *Mona Tykesson Klubien*: Livestock-MRSA in Danish pig farms (2021).
136. *Ove Njøten*: Comparing radar satellites. Use of Sentinel-1 leads to an increase in oil spill alerts in Norwegian waters (2021).
137. *Panagiotis Patrinos*: Change of heating fuel consumption patterns produced by the economic crisis in Greece (2021).
138. *Lukasz Langowski*: Assessing the suitability of using Sentinel-1A SAR multi- temporal imagery to detect fallow periods between rice crops (2021).
139. *Jonas Tillman*: Perception accuracy and user acceptance of legend designs for opacity data mapping in GIS (2022).
140. *Gabriela Olekszyk*: ALS (Airborne LIDAR) accuracy: Can potential low data quality of ground points be modelled/detected? Case study of 2016 LIDAR capture over Auckland, New Zealand (2022).
141. *Luke Aspland*: Weights of Evidence Predictive Modelling in Archaeology (2022).
142. *Luís Fareleira Gomes*: The influence of climate, population density, tree species and land cover on fire pattern in mainland Portugal (2022).
143. *Andreas Eriksson*: Mapping Fire Salamander (Salamandra salamandra) Habitat Suitability in Baden-Württemberg with Multi-Temporal Sentinel-1 and Sentinel-2 Imagery (2022).
144. *Lisbet Hougaard Baklid*: Geographical expansion rate of a brown bear population in Fennoscandia and the factors explaining the directional variations (2022).
145. *Victoria Persson*: Mussels in deep water with climate change: Spatial distribution of mussel (Mytilus galloprovincialis) growth offshore in the French Mediterranean with respect to climate change scenario RCP 8.5 Long Term and Integrated Multi-Trophic Aquaculture (IMTA) using Dynamic Energy Budget (DEB) modelling (2022).

146. *Benjamin Bernard Fabien Gérard Borgeais*: Implementing a multi-criteria GIS analysis and predictive modelling to locate Upper Palaeolithic decorated caves in the Périgord noir, France (2022).
147. *Bernat Dorado-Guerrero*: Assessing the impact of post-fire restoration interventions using spectral vegetation indices: A case study in El Bruc, Spain (2022).
148. *Ignatius Gabriel Aloysius Maria Perera*: The Influence of Natural Radon Occurrence on the Severity of the COVID-19 Pandemic in Germany: A Spatial Analysis (2022).
149. *Mark Overton*: An Analysis of Spatially-enabled Mobile Decision Support Systems in a Collaborative Decision-Making Environment (2022).
150. *Viggo Lunde*: Analysing methods for visualizing time-series datasets in open- source web mapping (2022).
151. *Johan Viscarra Hansson*: Distribution Analysis of Impatiens glandulifera in Kronoberg County and a Pest Risk Map for Alvesta Municipality (2022).
152. *Vincenzo Poppiti*: GIS and Tourism: Developing strategies for new touristic flows after the Covid-19 pandemic (2022).
153. *Henrik Hagelin*: Wildfire growth modelling in Sweden - A suitability assessment of available data (2023).
154. *Gabriel Romeo Ferriols Pavico*: Where there is road, there is fire (influence): An exploratory study on the influence of roads in the spatial patterns of Swedish wildfires of 2018 (2023).
155. *Colin Robert Potter*: Using a GIS to enable an economic, land use and energy output comparison between small wind powered turbines and large-scale wind farms: the case of Oslo, Norway (2023).
156. *Krystyna Muszel*: Impact of Sea Surface Temperature and Salinity on Phytoplankton blooms phenology in the North Sea (2023).
157. *Tobias Rydlinge*: Urban tree canopy mapping - an open source deep learning approach (2023).
158. *Albert Wellendorf*: Multi-scale Bark Beetle Predictions Using Machine Learning (2023).
159. *Manolis Papadakis*: Use of Satellite Remote Sensing for Detecting Archaeological Features: An Example from Ancient Corinth, Greece (2023).
160. *Konstantinos Sourlamtas*: Developing a Geographical Information System for a water and sewer network, for monitoring, identification and leak repair - Case study: Municipal Water Company of Naoussa, Greece (2023).
161. *Xiaoming Wang*: Identification of restoration hotspots in landscape-scale green infrastructure planning based on model-predicted connectivity forest (2023).
162. *Sarah Sienaert*: Usability of Sentinel-1 C-band VV and VH SAR data for the detection of flooded oil palm (2023).
163. *Katarina Ekeroot*: Uncovering the spatial relationships between Covid-19 vaccine coverage and local politics in Sweden (2023).
164. *Nikolaos Kouskoulis*: Exploring patterns in risk factors for bark beetle attack during outbreaks triggered by drought stress with harvester data on attacked trees: A case study in Southeastern Sweden (2023).
165. *Jonas Almén*: Geographic polarization and clustering of partisan voting: A local-level analysis of Stockholm Municipality (2023).
166. *Sara Sharon Jones*: Tree species impact on Forest Fire Spread Susceptibility in Sweden (2023).

167. *Takura Matswetu*: Towards a Geographic Information Systems and Data-Driven Integration Management. Studying holistic integration through spatial accessibility of services in Tampere, Finland. (2023).
168. *Duncan Jones*: Investigating the influence of the tidal regime on harbour porpoise Phocoena phocoena distribution in Mount's Bay, Cornwall (2023).
169. *Jason Craig Joubert*: A comparison of remote sensed semi-arid grassland vegetation anomalies detected using MODIS and Sentinel-3, with anomalies in ground-based eddy covariance flux measurements (2023).
170. *Anastasia Sarelli*: Land cover classification using machine-learning techniques applied to fused multi-modal satellite imagery and time series data (2024).
171. *Athanasios Senteles*: Integrating Local Knowledge into the Spatial Analysis of Wind Power: The case study of Northern Tzoumerka, Greece (2024).
172. *Rebecca Borg*: Using GIS and satellite data to assess access of green area for children living in growing cities (2024).
173. *Panagiotis – Dimitrios Tsachageas*: Multicriteria Evaluation in Real Estate Land-use Suitability Analysis: The case of Volos, Greece (2024).
174. *Hugo Nilsson*: Inferring lane-level topology of signalised intersections from aerial imagery and OpenStreetMap using deep learning (2024).
175. *Pavlos Alexantonakis*: Estimating lake water volume fluctuations using Sentinel-2 and ICESat-2 remote sensing data (2024).
176. *Karl-Martin Wigen*: Physical barriers and where to find them (2024).
177. *Martin Storsnes*: Temporal RX-algorithm performance on Sentinel-2 images (2024).